

Design of Ultrasonic Power Link for Neural Dust

Dongjin Seo



Electrical Engineering and Computer Sciences
University of California at Berkeley

Technical Report No. UCB/EECS-2016-21

<http://www.eecs.berkeley.edu/Pubs/TechRpts/2016/EECS-2016-21.html>

May 1, 2016

Copyright © 2016, by the author(s).
All rights reserved.

Permission to make digital or hard copies of all or part of this work for personal or classroom use is granted without fee provided that copies are not made or distributed for profit or commercial advantage and that copies bear this notice and the full citation on the first page. To copy otherwise, to republish, to post on servers or to redistribute to lists, requires prior specific permission.

Design of Ultrasonic Power Link for Neural Dust

by

Dongjin Seo

B.S. California Institute of Technology 2011

A thesis submitted in partial satisfaction
of the requirements for the degree of

Master of Science

in

Electrical Engineering and Computer Sciences

in the

GRADUATE DIVISION

of the

UNIVERSITY OF CALIFORNIA, BERKELEY

Committee in charge:

Professor Elad Alon, Chair
Professor Michel Maharbiz, Co-Chair

Spring 2014

Design of Ultrasonic Power Link for Neural Dust

Copyright © 2014

by

Dongjin Seo

Abstract

Design of Ultrasonic Power Link for Neural Dust

by

Dongjin Seo

Master of Science in Electrical Engineering and Computer Sciences

University of California, Berkeley

Professor Elad Alon, Chair

This report presents a new method of wireless power telemetry using ultrasound to power sub-mm sized neural implant called neural dust. It details the system design trade-offs and ultimate size, power, bandwidth scaling limits, as well as experimental results to verify the model framework. The proposed system improves the power transfer efficiency by up to 8 orders of magnitude compared to the traditional EM-based wireless powering at the same size scale and can be engineered to operate down to 10's μm scales. The extreme scalability of an ultrasound-based neural recording system makes it an attractive candidate for enabling a wireless interface to neural implants for applications such as brain-machine interfaces.

Contents

Contents	i
List of Figures	iv
1 Introduction	1
1.1 Motivation	1
1.2 Current State-of-the-art	2
1.3 Thesis Contribution	3
1.4 Thesis Organization	4
2 Wireless Power Transfer	6
2.1 Introduction	6
2.2 Electro-magnetic Power Transfer	7
2.2.1 Case Study: EM Link Efficiency	8
2.3 Ultrasonic Energy Transmission	10
3 Ultrasonic Link Design Considerations	12
3.1 Introduction	12
3.2 Generating Ultrasound	13
3.2.1 Piezoelectric Parameters	13
3.2.2 Piezoelectric Materials	16
3.3 Medical Ultrasound FDA Regulation	17
3.3.1 FDA Classification	17
3.3.2 Measuring Acoustic Output	17
3.3.3 Calculating FDA parameters	18
3.3.4 De-rating	19

3.4	Ultrasonic Link Model	20
3.4.1	Transducer model	20
3.4.2	Complete link model	23
3.4.3	Interrogator sizing	24
3.5	Simulation Results	25
3.6	Theoretical Scaling Limit	27
4	Experimental Verification	31
4.1	Introduction	31
4.2	Sample Preparation	31
4.2.1	Piezoelectric material	31
4.2.2	PZT dicing	32
4.2.3	Electrical connection	32
4.2.4	Post-processing PZT	33
4.3	Top Level Outline of Design	35
4.3.1	Electrical characterization	36
4.3.2	Ultrasonic characterization	39
4.4	Experimental Results	41
4.5	Summary	43
5	Conclusion	45
5.1	Thesis Summary	45
5.2	Future Directions	46
	References	48
	References	48
	Acknowledgements	52
A	Appendix	53
A.1	Table of Piezoelectric Materials	53
A.2	Process Debugging	53
A.2.1	Electroplating	53
A.2.2	PZT dicing	53
A.3	Measurement Setup	54

A.3.1	Hydrophone measurement	55
A.3.2	Power transfer measurement	55

List of Figures

1.1	Neural dust system diagram showing the placement of ultrasonic interrogator under the skull and the independent neural dust sensing nodes dispersed throughout the brain.	4
2.1	Total channel loss in 2 mm brain tissue, due to both tissue and propagation loss, increases exponentially with frequency.	9
2.2	The mutual coupling, and therefore link efficiency, also reduces dramatically with the scaling of chiplet dimensions.	9
2.3	Comparison of both the scale and the loss incurred in brain tissue between ultrasound and EM radiation, displaying the stark differences in the achievable spatial resolution (set by the wavelength) and the tissue/path loss for operating frequency of a 100 μm neural dust (*Attenuation of ultrasound in brain is 0.5 dB/(cm·MHz))	11
3.1	FDA regulatory limits	20
3.2	KLM model of a neural dust piezoelectric transducer, showing one electrical port and two mechanical ports. Coupling between the domains is modeled with an ideal electromechanical transformer.	21
3.3	COMSOL simulation exhibits a resonant shift and spurious tones present in the frequency spectra of a cube transducer.	22
3.4	Complete single interrogator, single neural dust power and communication link models.	23
3.5	Link efficiency as a function of the neural dust side dimension.	26
3.6	Comparison of link efficiency via EM and ultrasound indicates that for implants smaller than $\sim 1 \text{ mm}^2$, ultrasonic power transfer outperforms EM significantly.	27
3.7	As we scale down neural dust dimension, more power is needed to keep the noise floor down to maintain SNR while less power is captured. The intersection of these two trends is the smallest node that will still operate. The analysis assumes the use of PZT, two different FDA-approved ultrasonic power transfer protocols.	28

3.8	Neural dust with an ultra-compliant flexible polyimide “tail”, populated with recording sites, can be envisioned to bypass the limits of the achievable differential signal between two electrodes placed on a neural dust footprint and to extend the scaling limit.	29
4.1	Assembly prototype schematic and PCB board for the experiments.	34
4.2	The processing steps ensure that the desired PZT dimension is assembled on the test board.	35
4.3	Measurement diagram for electrical impedance measurement with VNA.	36
4.4	Before (top) and after (bottom) calibrating out the board.	37
4.5	Measured impedance spectroscopy of a PZT crystal matches simulation.	38
4.6	Cross section of an ultrasonic transducer	39
4.7	Acoustic characterization setup with a calibrated ultrasonic transducer for power delivery verification	40
4.8	The output power of a 5 MHz transducer as the hydrophone is moved away from the transducer’s surface. The de-rated peak is shifted to the left in relation to the water peak.	40
4.9	The XZ cross-section of the transducer output illustrates a Rayleigh distance and a clear transition from the near-field to far-field propagation.	42
4.10	The XY beam cross-section shows 6 dB bandwidth of the beam at 2.2 mm.	43
4.11	Measured power transfer efficiency at various neural dust sizes matches simulated behavior closely.	44
4.12	Frequency response of harvested power on the PZT reinforces the reliability of the simulation framework.	44
A.1	Table of Piezoelectric Materials	54
A.2	Troubleshooting for electroplating	54
A.3	Pieces of crystal bond surrounding the solderpaste (underneath the PZT sheets) pre-bake.	55
A.4	Experimental stations for measuring neural dust power transfer efficiency (left) and transducer characterization (right).	56
A.5	Ultrasonic transducer and the hydrophone are immersed in a water tank and mounted on 3-axis linear, computer-controlled and manual stages, respectively, for XYZ beam scanning.	56
A.6	1 - 20 MHz broadband hybrid capsule hydrophone has an active area of 400 μm at the tip, with 160 nV/Pa conversion. The hydrophone is attached to a switchable gain amplifier to increase its dynamic range.	57

A.7	The top view of the alignment of transducer to the hydrophone in the water tank. Due to the small aperture size of the hydrophone, the measurements are extremely vibration sensitive. Cautionary measures, such as using a vibration isolation workbench or pads, must be considered.	57
A.8	A programmable function generator (in yellow) and radio frequency (RF) amplifier (in blue) were used to drive the ultrasonic transducer. The harvest voltage was displayed on the oscilloscope (in red).	58
A.9	The transducer is mounted on a computer-controlled 2-axis translating stage such that the transducer could be immersed in the water at a distance of approximately 30 mm directly above the sample.	58
A.10	Assembly prototype (PZT crystal in yellow) is placed in a water container and the power harvested by the piezo is displayed on an oscilloscope (not shown).	59

Chapter 1

Introduction

1.1 Motivation

Significant progress has occurred in the field of brain-machine interfaces (BMI) since the first demonstration that prosthetic devices can be directly controlled with signals from cortical neurons in rodents [1]. Since then, a productive decade full of exciting proof-of-concept experiments on animal subjects ([2] - [5]) has poised BMI technology as a potential new therapy to greatly improve the quality of life of millions of people suffering from spinal cord injury, stroke, and other debilitating neurological conditions. In order to realize such clinically viable BMI systems that can restore movement by transforming thought into action and allow a patient to perform tasks of daily living in a natural and effortless way, two major challenges remain: 1) engineering fully implantable neural interfaces that last a lifetime and 2) achieving a level of control and dexterity of the prosthetic device that will justify the risk/benefit ratio of having such a device implanted.

The first challenge concerns all aspects of the implantable device, such as addressing performance degradation due to biotic and abiotic effects associated with inserting implants, the density and spatial coverage of the sensing sites, the type of signals measured, and the computation and communication capabilities under the power budget of the whole system [6]. The second challenge on the other hand gravitates more towards improving

decoding algorithms to provide a more accurate and a higher level of control, multiple artificial feedback signals to assimilate the prosthetic limb in the brain representation, and encoding of sensory feedback from the prosthetic device by directly stimulating sensory areas in the brain [7], [8].

Addressing these important challenges is critical for BMIs to have a broad and important clinical impact. In this thesis, we focus on the first challenge, specifically on introducing a new technology that will radically increase the number of recording sites from the brain while eliminating trans-cranial wires and aiming to enable lifetime-scale operation.

1.2 Current State-of-the-art

Currently, the majority of neural recording is done through the direct electrical measurement of potential changes near relevant neurons during depolarization events called action potentials (AP). Additionally, there are numerous clinically useful modalities with which one can extract information from the brain. Advances in imaging such as functional magnetic resonance imaging (fMRI), electroencephalograph (EEG), positron emission tomography (PET) and magnetoencephalograph (MEG), have provided a wealth of information about collective behaviors of groups of neurons. Numerous efforts are focusing on intra- and extra-cellular electrophysiological recording/stimulation, optical recording, optogenetic stimulation, opto-electrical and electroacoustic methods to perturb and record the individual activity of neurons in large (and, hopefully scalable) ensembles. All modalities have some fundamental trade-off and are usually limited in temporal or spatial resolution, portability, power, invasiveness, etc. [9]

While the specifics vary across several prominent technologies, all extracellular electrical recording interfaces share several characteristics:

- Wired or wireless electrical connection between the active area inside the brain and electronic circuits outside the skull [10]- [13]
- A practical upper bound of several hundred implantable recording sites [14]- [16]

- The development of a biological response around the implanted electrodes which degrades recording performance over time [17]- [20]

To date, clinical neural implants have proved to be successful in the short term (months to a few years) and for a small number of channels (10's to 100's) [21]. Chronic recording (a decade or more) and recording from thousands of sites in a clinically relevant manner with little or no tissue response would be a game changer.

This begs the question: Is there a way to embed very tiny recording devices in the brain such that we could radically increase the number of recording sites while eliminating trans-cranial wires and enabling lifetime-scale operation?

1.3 Thesis Contribution

We introduce an ultra-miniature as well as extremely compliant system shown in Figure 1.1 that enables massive scaling in the number of neural recordings from the brain while providing a potential path towards truly chronic BMI [6]. This is achieved via two fundamental technology innovations: 1) 10 – 100 μm scale, free-floating, independent sensor nodes, or *neural dust*, that can detect and report local extracellular electrophysiological data at a single neuron level, and 2) *sub-cranial mm-scale ultrasonic interrogators* that establish power and communication links with the neural dust. The interrogators are placed beneath the skull and below the dura mater in order to avoid strong attenuation of ultrasound by bone, and are powered by an external transceiver based on electromagnetic power transfer.

In this thesis, we focus particularly on the technical rational for *why* and *how* ultrasound can deliver sufficient power to sub-mm sized neural implants to provide a toolset from which to build scalable, chronic extracellular recording systems.

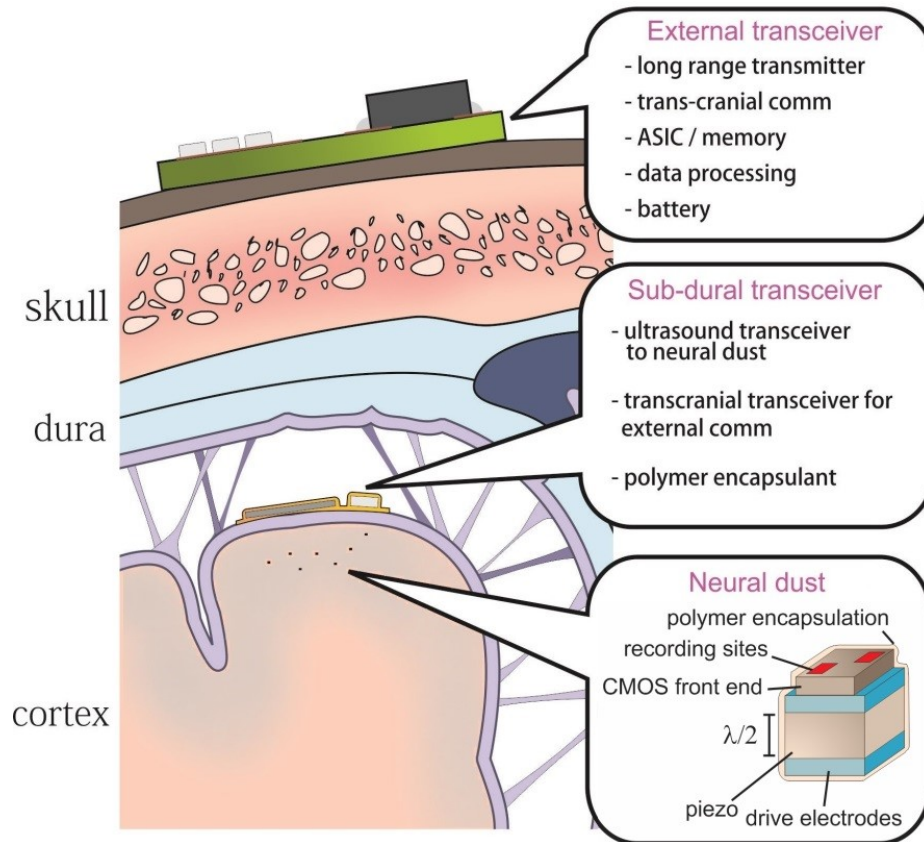


Figure 1.1. Neural dust system diagram showing the placement of ultrasonic interrogator under the skull and the independent neural dust sensing nodes dispersed throughout the brain.

1.4 Thesis Organization

The rest of this thesis is organized as follows. Chapter 2 provides an overview of various wireless power transfer techniques and introduces ultrasound as an alternative option for brain-machine interfaces. Comparative analysis of wireless power-transfer efficiency and limitations is presented. Based on the findings of Chapter 2, key parameters to model and achieve high-efficiency ultrasonic links are introduced and analyzed in Chapter 3. The simulation results of the overall system, under the safety regulation set by health concerns and the overall link efficiencies, are presented with comments about the scaling of the system architecture. The process flow to fabricate and test a proof-of-concept sub-mm $(127 \mu\text{m})^3$

node is detailed in Chapter 4. The measurement setup and results are also included in this chapter. Finally, the results are summarized in Chapter 5 and some directions for future research are suggested.

Chapter 2

Wireless Power Transfer

2.1 Introduction

The requirements for any electronic platform interfacing with microelectrodes to acquire useful neural signals are fairly stringent. The two primary constraints on the implanted device are size and power. On one hand, implants placed into cortical tissue with scales larger than one or two cell diameters have well-documented tissue responses which are ultimately detrimental to performance. On the other hand, reducing the size of implants reduces the distance between recording points, which decreases the absolute magnitude of the measured potentials. This decreased amplitude necessitates reductions in the front-end noise, which in turns requires higher power (i.e., for a fixed bandwidth, lowering the noise floor requires increased power consumption).

Smaller devices, however, collect less power, and building sufficiently low-power electronics may be extremely challenging. Additionally, to eliminate the risk of infection associated with the transcutaneous/trans-cranial wires required for communication and power, such tethers should be avoided as much as possible; a wireless hub is therefore essential to relay the information recorded by the device through the skull.

Several energy modalities exist for powering and communicating with implants and recently, implantable wireless neural interfaces have been demonstrated in an effort to extend

system longevity. In this chapter, we will review one common method of wireless power transfer, its use as well as limitations for neural dust, and offer an alternative solution.

2.2 Electro-magnetic Power Transfer

The most popular existing wireless power transfer technique relies on electromagnetics (EM) as the energy modality [22]. An external transmitter generates and transfers information through purely electric [23] or magnetic [24] near field or electromagnetic far field coupling [25]; this energy can be harvested by the implanted device and converted into a stable DC supply voltage. Energy transmission via magnetic near field has been used in a wide variety of medical applications and is the principal source of power for cochlear implants [26]. As EM requires no moving parts or the need for chemical processing or temperature gradients, it is considered more robust and stable than other forms energy scavenging.

When used in-body, however, EM coupling power density is restricted by the potential adverse health effects associated with excess tissue heating in the vicinity of the human body due to electromagnetic fields. This is regulated by the well-known FCC and IEEE-recommended levels [27]. Roughly, the upper limit for EM power density transiting through tissue is set by the requirement to not heat a model sample of human tissue by more than 1°C. For electromagnetic waves, the output power density is frequency dependent and cannot exceed a maximum of 10 mW/cm².

Consider, in this context, the problem of transmitting EM power to a very small implant embedded in tissue with the following specifications:

Implant (RX) size	100 μm^2
Interrogator (TX) size	1 mm^2
Transmission distance	2 mm
Transmission medium	Brain tissue

In particular, as a comparative measure, in this section, we are interested in:

- What is the achievable power transfer efficiency?
- What is the absolute maximum power we can harvest at the implant?
- Does this approach scale to allow high density neural recordings?

2.2.1 Case Study: EM Link Efficiency

One possible implementation of an implant which is capable of coupling to the EM waves contains a resonant component. Such a system can be modeled as a series/parallel RLC where for the purpose of this exercise, one may presume that a suitable method exists for modulating the quality factor or mutual coupling of the RLC as a function of neural activity. Assume that the TX and RX coils are perfectly aligned and that an implant can accommodate capacitance density of approximately $10 \text{ fF}/\mu\text{m}^2$ and a planar square loop inductor with the inductance determined by,

$$L = \frac{1.27 \cdot \mu_o n^2 d_{avg}}{2} \left[\ln\left(\frac{2.07}{\phi}\right) + 0.18\phi + 0.13\phi^2 \right] \quad (2.1)$$

where n is the number of turns, d_o and d_i are the outer and inner diameter of the coil, respectively, $d_{avg} = \frac{d_o + d_i}{2}$ and ϕ is a parameter known as fill factor, defined as $\frac{d_o - d_i}{d_o + d_i}$ [28]. In order to compute the expression for the efficiency of the EM link, it can be shown mathematically that (derivation can be found in [29]),

$$\eta = \frac{k^2 Q_{TX} Q_L}{1 + k^2 Q_{TX} Q_L} \cdot \frac{Q_L}{Q_{RX} + Q_L} \quad (2.2)$$

where k is the coil coupling coefficient defined as $\frac{M}{L_{TX} + L_{RX}}$, M is the coil mutual inductance, L_{TX} and L_{RX} are the inductances of TX and RX, respectively, Q_{TX} is the unloaded quality factor of the TX coil, Q_{RX} is the unloaded quality factor of the RX coil, and Q_L is the loaded quality factor of the RX coil.

Additionally, the attenuation of the EM signal as it propagates through brain tissue due to tissue absorption is well documented [27] and the parameters can be extracted to model the transmission channel. Figure 2.1 plots the modeled channel loss as a function of

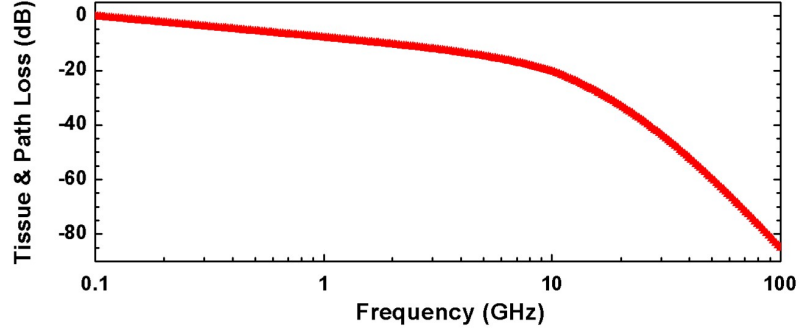


Figure 2.1. Total channel loss in 2 mm brain tissue, due to both tissue and propagation loss, increases exponentially with frequency.

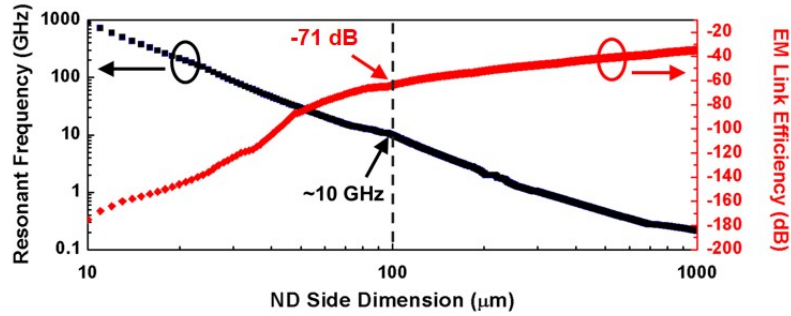


Figure 2.2. The mutual coupling, and therefore link efficiency, also reduces dramatically with the scaling of chiplet dimensions.

frequency and includes loss from tissue absorption as well as path loss (or beam spreading) based on the Friis equation: $20\log(\lambda/(4\pi r))$ where λ is λ_{tissue} .

An iterative solver that optimizes η in this channel was written in MATLAB and the calculations predict that the resonant frequency of a 100 μm neural dust would be ~ 10 GHz. We observe that there is an exponential relationship between the channel loss and the frequency, and at 10 GHz – the total combined loss for one-way transmission is approximately 20 dB.

Furthermore, as shown in Figure 2.2, scaling down the dimensions of the implants increases the resonant frequency of the link, causing an exponential increase in the tissue absorption loss and the overall channel loss, and the efficiency of EM transmission becomes

miniscule. Specifically, EM transmission with a $100\ \mu\text{m}$ neural dust embedded 2 mm into the cortex results in 71 dB of transmission loss. Given a $1\ \text{mm}^2$ transmitter aperture outputting $100\ \mu\text{W}$ of power limited by the need to satisfy safety regulations on output power density of $10\ \text{mW}/\text{cm}^2$ – the resulting received power at the neural dust is $\sim 8\ \text{pW}$. This is orders of magnitude smaller than the power consumption imposed by noise requirements on the front-end amplification circuitry, and as a result, prior work by [10], which features the most energy-efficient and smallest wirelessly EM powered neural recording system to date, at $2.5\ \mu\text{W}/\text{channel}$ and $250\ \mu\text{m} \times 450\ \mu\text{m}$, is limited in terms of further dimensional scaling and increasing the range (the effective range within brain tissue for this work was 0.6 mm). Due to the non-linear interplay of form factor, speed of light, and frequency spectra of tissue absorption, EM energy transmission is not an appropriate energy modality for the powering of 10's of μm sized neural dust implants.

2.3 Ultrasonic Energy Transmission

Ultrasonic transducers have found application in various disciplines including imaging, high intensity focused ultrasound (HIFU), nondestructive testing of materials, communication and power delivery through steel walls, underwater communications, transcutaneous power delivery, and energy harvesting [30]- [33]. The idea of using acoustic waves to transmit energy was first proposed in 1958 by Rosen [34] to describe the energy coupling between two piezoelectric transducers. Unlike electromagnetics, using ultrasound as an energy transmission modality never entered into widespread consumer application and was often overlooked because the efficiency of electromagnetics for short distances and large apertures is superior. However, at the scales discussed here and in tissue, the low acoustic velocity allows operation at dramatically lower frequencies, and more importantly, the acoustic loss in tissue is generally substantially smaller than the attenuation of electromagnetics in tissue (Table 2.3).

The relatively low acoustic velocity of ultrasound results in substantially reduced wavelength compared to EM. For example, 10 MHz ultrasound in brain tissue has a wavelength

	Ultrasound	EM
λ in brain tissue	150 μm @ 10 MHz	5 mm @ 10 GHz
Tissue & path loss at 2 mm	1 dB*	20 dB

Figure 2.3. Comparison of both the scale and the loss incurred in brain tissue between ultrasound and EM radiation, displaying the stark differences in the achievable spatial resolution (set by the wavelength) and the tissue/path loss for operating frequency of a 100 μm neural dust (*Attenuation of ultrasound in brain is 0.5 dB/(cm·MHz))

$\lambda = 150 \mu\text{m}$, while for 10 GHz EM, $\lambda = 5 \text{ mm}$ [35]. This smaller wavelength implies that for the same transmission distance, ultrasonic systems are much more likely to operate in the far-field, and hence obtain larger spatial coverage than an EM transmitter.

More importantly, the acoustic loss in brain tissue is fundamentally smaller than the attenuation of electromagnetics in tissue because acoustic transmission relies on compression and rarefaction of the tissue rather than time-varying electric/magnetic fields that generate displacement currents on the surface of the tissue [36]. This is also manifested by the stark difference in the time-averaged acceptable intensity for ultrasound for cephalic applications, regulated by FDA, which is approximately 72x (720 mW/cm²) more than EM for devices conforming to output display standards (ODS) (recall EM is limited to 10 mW/cm²) [37].

At a first glance, ultrasound appears attractive for in-tissue communication given its short wavelength and low attenuation. The analysis of key parameters to model and achieve high-efficiency ultrasonic links is detailed in the following chapter.

Chapter 3

Ultrasonic Link Design Considerations

3.1 Introduction

Piezoelectricity refers to the phenomenon present in certain solid (usually crystalline) materials where there is an interaction between the mechanical and electrical states. As a result, piezoelectric materials can transduce electrical energy into mechanical energy and vice versa by changing lattice structure, and this state change is accessible via either electrical stimulation or mechanical deformation.

These materials serve as a critical component in the construction of probes that generate ultrasonic waves to enable ultrasound technology used in the medical industry. A relatively wide range of piezoelectric materials are available, each suitable for different applications. In this chapter, we will survey different piezoelectric materials and discuss their use cases based on piezoelectric properties.

3.2 Generating Ultrasound

3.2.1 Piezoelectric Parameters

For a crystal to exhibit the piezoelectric effect, its structure should have no center of symmetry, or must be anisotropic. In other words, a stress (tensile or compressive) applied to such a crystal will alter the separation between the positive and negative charge sites in each elementary cell leading to a net polarization at the crystal surface. The effect is practically linear and in linear elastic solids, the strain (S) and stress (T) are related by the elastic stiffness (c). In the same material, the electric displacement (D) is related to the electric field (E) by the permittivity (ϵ_r) of the material. The constitutive equations for a piezoelectric material are,

$$T = cS + hE \quad (3.1)$$

$$D = \epsilon_r E + hS \quad (3.2)$$

where h is the piezoelectric coupling coefficient.

This section provides information about the main parameters that need to be used to compare different piezoelectric materials while selecting for a particular application.

Piezoelectric strain constant (symbol: d , unit: m/V)

Piezoelectric strain constants, or the d coefficients, indicate the mechanical strain (S) experienced by a piezoelectric material per unit of electric field applied (E).

$$d = \frac{S}{E} \quad (3.3)$$

By definition, large d_{ij} constants correspond to generation of higher mechanical strain (or mechanical displacements) for given electric field. As a result, the d coefficients are important for assessing a material's ability to cause strain/actuate and is often termed the transmitting constants. The first subscript to d indicates the direction of applied field strength while the second subscript describes the induced strain.

Piezoelectric voltage constant (symbol: g , unit: Vm/N)

Piezoelectric voltage constants, or the g coefficients, indicate the electric field (E) generated by a piezoelectric material per unit of mechanical stress (T) applied,

$$g = \frac{E}{T} \quad (3.4)$$

By definition, higher value of g corresponds to generation of higher electric field across a piezoelectric material for given mechanical stress. As a result, the g coefficients are important for assessing a material's ability to sense and is often termed the receiving constants. The first subscript to g indicates the direction of the electric field generated in the material while the second subscript describes the direction of the applied stress.

Electromechanical coupling factor (symbol: k , unitless)

The coupling coefficient (sometimes referred to as the electromechanical coupling coefficient) is defined as the ratio of the mechanical energy accumulated in response to an electrical input or vice versa. The piezoelectric coupling coefficient can be expressed in the following equations:

$$k^2 = \frac{\text{energy converted}}{\text{input energy}} = \frac{\pi f_r}{2 f_a} \cot\left(\frac{\pi f_r}{2 f_a}\right) \quad (3.5)$$

where f_r and f_a represent resonant (where the impedance is minimized) and anti-resonant frequency (where the impedance is maximized) of the piezoelectric material, respectively.

Based on resonance mode, different electromechanical coupling factors can be defined:

- k_{33} : factor for electric field in direction 3 (parallel to direction in which ceramic element is polarized) and longitudinal vibrations in direction 3 (ceramic rod, length $\geq 10 \times$ diameter)
- k_t : factor for electric field in direction 3 and vibrations in direction 3 (thin disc, surface dimensions large relative to thickness; $k_t < k_{33}$)

- k_{31} : factor for electric field in direction 3 (parallel to direction in which ceramic element is polarized) and longitudinal vibrations in direction 1 (perpendicular to direction in which ceramic element is polarized) (ceramic rod)
- k_p : factor for electric field in direction 3 (parallel to direction in which ceramic element is polarized) and radial vibrations in direction 1 and direction 2 (both perpendicular to direction in which ceramic element is polarized) (thin disc)

Thickness mode frequency constant (symbol: N_t , unit: Hz-m)

The thickness mode frequency constant, N_t , is related to the thickness of the ceramic element, t , by $N_t = f_s t$, where f_s is series resonance frequency. This is used to calculate the frequency of operation.

Mechanical quality factor (symbol: Q_m , unitless)

This corresponds to selectiveness of PZT with applied electric field frequency. It can be expressed as:

$$Q_m = \frac{f_a^2}{2\pi f_r Z_r C_p (f_a^2 - f_r^2)} \quad (3.6)$$

where f_r and f_a represent resonant and anti-resonant frequency, respectively, Z_r represents an impedance at resonance, and C_p is the low-frequency capacitance. In general, in a datasheet, the provided value corresponds to Q_m in air.

Dielectric dissipation factor (symbol: $\tan\delta$, unitless)

This corresponds to dielectric loss in the PZT and should be kept low to reduce heat loss in the piezoelectric material for implant applications.

Permittivity (symbol: ϵ_{ij} , unitless)

The permittivity (or dielectric constant) is defined as the dielectric displacement per unit electric field. The first subscript gives the direction of the dielectric displacement and the second gives the direction of the electric field.

Curie temperature (symbol: T_c , unit: °C)

The temperature at which the crystal structure changes from a non-symmetrical (piezoelectric) to a symmetrical (non-piezoelectric) form.

3.2.2 Piezoelectric Materials

There are several types of piezoelectric materials available and each type is tailored towards the requirements of particular applications. For instance, there are piezoelectric ceramic compounds (such as lead zirconate titanate or PZT) which have low internal loss mechanisms (high Q) due to crystal structural deformation within the ceramics. The hard nature of these materials allows high electric field to create a large displacement between dipoles on the material. Consequently, ceramics are very efficient at converting an applied electrical voltage into pressure (have high d -coefficient) and are popular choices for the generation of high-power, narrowband ultrasonic signals for therapeutic ultrasound.

On the other hand, there are piezoelectric polymer compounds (such as polyvinylidene (di)fluoride or PVDF) which are inherently low Q materials. The compliant nature of the polymers makes it easy for the pressure impinging on it to disperse its energy to dipoles on the material. Consequently, polymers have high g -coefficients and are primarily used to construct broadband, high-sensitivity hydrophones.

In the context of an implant, the lead content of PZT makes it difficult to introduce into human tissue in chronic applications. Several works have demonstrated encapsulation as an option to avoid this issue [38], [39], but the long-term stability of such encapsulation layers remain to be investigated. Luckily, biocompatible piezoelectric materials (such as barium titanate or BaTiO₃) exist with properties similar, but generally inferior to PZT. A table of piezoelectric properties of these materials can be found in the Appendix A.

3.3 Medical Ultrasound FDA Regulation

Clinical uses of ultrasound are known to have the potential to create two major types of bio-effects: thermal heating of tissue from the absorption of ultrasound in the body, and mechanical effects such as cavitation. In order to ensure safety of medical ultrasound systems, hard limits are imposed on the acoustic output power of U.S. systems by the Food and Drug Administration (FDA). This section introduces some of the relevant parameters and their definitions. A detailed account of the rationale and derivation of all parameters can be found in [37].

3.3.1 FDA Classification

The FDA uses a 2-track approach to marketing clearance: track 1 and track 3. Track 1 is for devices that do not follow the Output Display Standard (ODS), which requires an imaging system to provide users with direct on-screen estimates of relative thermal and mechanical indices related to these two bio-effects. As a result, track 1 has application-specific output limits. On the other hand, track 3 is for devices that conform to the ODS and is not determined on an application-specific basis.

3.3.2 Measuring Acoustic Output

The radiation pattern and pressure fields generated by the ultrasonic transducers can be characterized using miniature sensors called hydrophones. Hydrophones operate purely as a receiver of ultrasound and consist of thin plates or films of piezoelectric material fabricated in the form of small sensing elements which convert the incident acoustic pressure waveform into an electric signal. As described in the previous section, in order to achieve sufficient sensitivity to produce a reasonable signal level and enough bandwidth to cover the desired frequency range, piezoelectric polymers such as polyvinylidene (di)fluoride (PVDF) with high g constant are used as the sensing element.

There are two main types of hydrophones: needle and membrane hydrophones. Needle

hydrophones are constructed from a small disc of a piezoelectric material mounted on the end of a coaxial conductor. Due to their small cross-sectional area and minimal reflection from the probe, needle hydrophones are well suited for continuous wave applications. On the other hand, membrane hydrophones are constructed from one or more very thin layers of the piezoelectric material stretched taut within a frame. The piezopolymer has to be carefully prepared so that only a small region in the middle of the film is piezoelectrically active. Due to their smoothly varying frequency response over a very broad frequency range, they are well suited to characterize broadband short pulses that are produced by ultrasonic imaging systems. In general, membrane hydrophones are more costly and less rugged compared to the needle hydrophone. Hybrids of the two, such as capsule hydrophones, also exist and exhibit a flat sensitivity comparable to membrane hydrophones with a good reflection profile that does not affect the acoustic field.

3.3.3 Calculating FDA parameters

In a typical ultrasonic imaging system, short pulses of ultrasonic energy are reflected back toward the transducer from interfaces having different acoustic properties. Due to this pulse-based measurement, there are several different parameters of acoustic output intensity. Most notably:

- I_{SPTA} : spatial-peak temporal-average intensity describes the highest intensity measured at any point in the ultrasound beam averaged over the pulse repetition period.
- I_{SPPA} : spatial-peak pulse-average intensity describes the highest intensity measured at any point in the ultrasound beam averaged over the time duration of the pulse.

In order to compute I_{SPTA} and I_{SPPA} , we must first calculate the pulse intensity integral (PII), which is defined as,

$$PII = 0.1 \cdot \int \frac{p^2(t)}{Z_0} dt \text{ (in } mJ/cm^2 \text{)} \quad (3.7)$$

where p is the instantaneous peak pressure (in Pa), Z_0 is the characteristic acoustic impedance (in $Pa \cdot s^{-1}$ or Rayl) defined as ρc where ρ is the density of the medium and c

is the speed of sound in the medium. Given PII, both I_{SPTA} and I_{SPPA} can be calculated from,

$$I_{SPPA} = \frac{PII}{PD} \text{ (in } mW) \text{ and } I_{SPTA} = PII(PRFF) \text{ (in } mW) \quad (3.8)$$

where PRF is defined as pulse repetition frequency (in Hertz) and PD is the pulse duration (in sec) defined as times it takes to reach $0.9 \cdot PII$ from $0.1 \cdot PII$ multiplied by a constant (i.e., $(0.9 \cdot PII - 0.1 \cdot PII) \cdot 1.25$) as outlined by technical standards established by the American Institute for Ultrasound in Medicine and National Electronics Manufactures Administration [37].

3.3.4 De-rating

The majority of hydrophone measurements are performed in water, which exhibits an attenuation coefficient of $0.0022 \text{ dB/cm} \cdot (f/1 \text{ MHz})^2$. However, since tissue attenuates ultrasound more significantly, the maximum value of the pressure anywhere in the ultrasound field measured in water is reduced by an attenuation factor which ranges from $0.3 \text{ dB}/(\text{cm} \cdot \text{MHz})$ to $1.2 \text{ dB}/(\text{cm} \cdot \text{MHz})$ [37]. In order to capture the worst-case scenario, de-rating describes a process of re-calculating pressure produced in a homogenous tissue model with an attenuation coefficient of $0.3 \text{ dB}/(\text{cm} \cdot \text{MHz})$ (the lowest bound for worst-case). Attenuated output intensities are denoted by the subscript “.3” (i.e., $I_{SPTA,3}$). All of the FDA regulatory levels are specified with de-rated values.

Once the de-rated output levels are determined, the total integrated output power from the transducer can be calculated by,

$$W_0 = A_{eq} I_{SPTA} = \frac{\pi d_{-6}^2}{4} I_{SPTA} \text{ (in } mW) \quad (3.9)$$

where the equivalent beam area (A_{eq}) can be approximated as a circle with a diameter d_{-6} , which is the -6 dB beam diameter. Given that the power required to cause a 1°C temperature rise at the surface is,

$$W_{deg} = \frac{210}{f_{awf}} \text{ (in } mW) \quad (3.10)$$

	$I_{SPTA,3}$ (mW/cm ²)	$I_{SPPA,3}$ (mW/cm ²)	TIS	MI
Track 1 (Cephalic Application)	< 94	< 190,000	< 6	< 1.9
Track 3	< 720	< 190,000	< 6	< 1.9

Figure 3.1. FDA regulatory limits

where f_{awf} is the acoustic working frequency (in MHz), we can calculate thermal index at the surface of the tissue (TIS) as,

$$TIS = \frac{W_0}{W_{deg}} = \frac{W_0 f_{awf}}{C_{TIS1}} \quad (3.11)$$

where $C_{TIS1} = 210 \text{ mW}\cdot\text{MHz}$.

Finally, the mechanical index, which determines the likelihood of cavitation caused by bubble formation in a liquid material when the local pressure produced by the rarefaction part of a passing ultrasound wave falls below the vapor pressure of the liquid sufficient to pull the material apart, can be calculated as,

$$MI = \frac{p_{r,3}}{\sqrt{f_{awf}}} \quad (3.12)$$

where $p_{r,3}$ is the de-rated peak rarefactional pressure. Table 3.1 below shows a summary of FDA limits for the following parameters under the two different tracks.

3.4 Ultrasonic Link Model

3.4.1 Transducer model

The design of neural dust is heavily constrained in both size and available power to the implant. As a result, it is imperative to accurately model the transmission channel to maximize the power efficiency. Therefore, this section elaborates design tradeoffs and methodologies for power delivery optimization.

Due to the importance of piezoelectric transducers in various applications, a number of models of the electromechanical operation of one-dimensional piezoelectric and acoustic

phenomena have evolved over the years. The KLM model is arguably the most common equivalent circuit and is a useful starting point to construct a full link model with the intent of examining scaling and system constraints [40]. The basic model includes a piezoelectric transducer with electrodes fully covering the two largest faces of the transducer. The entire transducer is modeled as a frequency-dependent three-port network, consisting of one electrical port (where electric power is applied or collected) and two acoustical ports (where mechanical waves are produced or sensed from the front and back faces of the transducer). The parallel-plate capacitance due to the electrodes and the frequency-dependent acoustic capacitance are modeled as C and X_i , respectively, and the transduction between electrical and mechanical domains is modeled as an ideal electromechanical transformer with a turn ratio of Φ , connected to the middle of a transmission line of length $\lambda/2$, as shown in Figure 3.2. Assuming an infinite 2D plate piezoelectric transducer of thickness h , the resonant frequency is set by $h = \lambda/2$; at the resonant frequency, the ultrasound wave impinging on either the front or back face of the transducer will undergo a 180° phase shift to reach the other side, causing the largest displacement between the two faces. This observation implies that phase inversion only exists at the odd harmonics of the fundamental mode in a given geometry.

The KLM model, however, was derived under the assumption of pure one-dimensional thickness vibration, and therefore can only provide a valid representation for a piezoelectric transducer with an aspect ratio (width/thickness) greater than 10 that mainly resonates

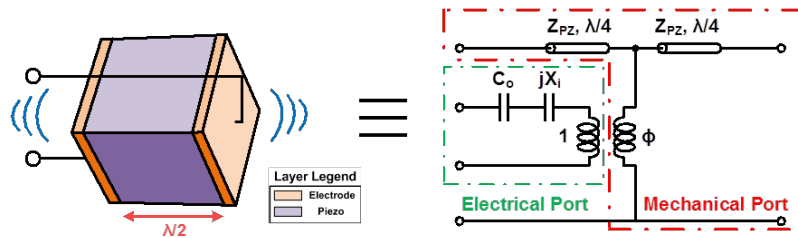


Figure 3.2. KLM model of a neural dust piezoelectric transducer, showing one electrical port and two mechanical ports. Coupling between the domains is modeled with an ideal electromechanical transformer.

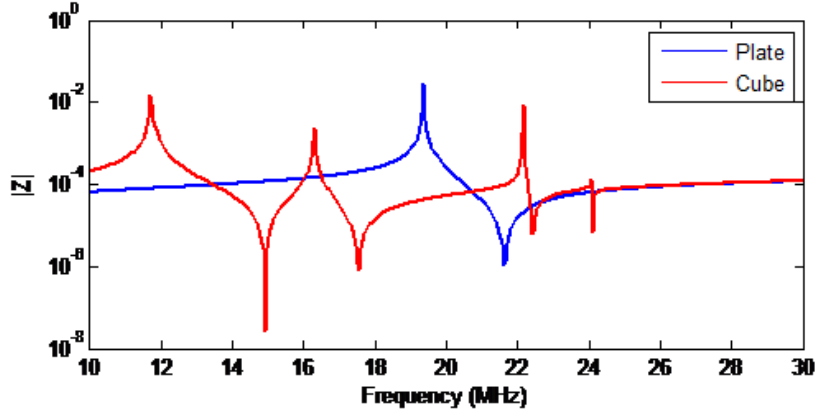


Figure 3.3. COMSOL simulation exhibits a resonant shift and spurious tones present in the frequency spectra of a cube transducer.

in the thickness mode [41]. Given the extreme miniaturization target for the neural dust, a cube dimension (aspect ratio of 1:1:1) is a better approximation of the geometry than a plate (aspect ratio $> 10:10:1$). Due to Poisson's ratio and the associated mode coupling between resonant modes along each of the three axes of the cube, changing aspect ratio alters the resonant frequencies [42]. The piezoelectric transducers for both the interrogator and the neural dust must be designed to resonate at the same frequency to maximize the link efficiency. In this model, we assume the neural dust nodes are cubic and the external transceiver is approximately planar (i.e., 2D).

In order to obtain KLM parameters for the neural dust transducer, we simulated a cube transducer using a 3D finite element package (COMSOL Multiphysics) to model both the resonant frequency shift vs. a plate and the manifestation of spurious tones and higher resonances of a $100 \mu\text{m}$ thick PZT as shown in Figure 3.3. The effect of decrease in resonance by a factor of 1.5 is included in the KLM model by extracting the effective acoustic impedance of the neural dust from the COMSOL model. To match the resonant frequency of the interrogator and the neural dust, the interrogator thickness is varied to match the fundamental thickness mode of the neural dust. Approximately 66 % of the total output energy is contained in the main thickness resonance; this is modeled as a loss term.

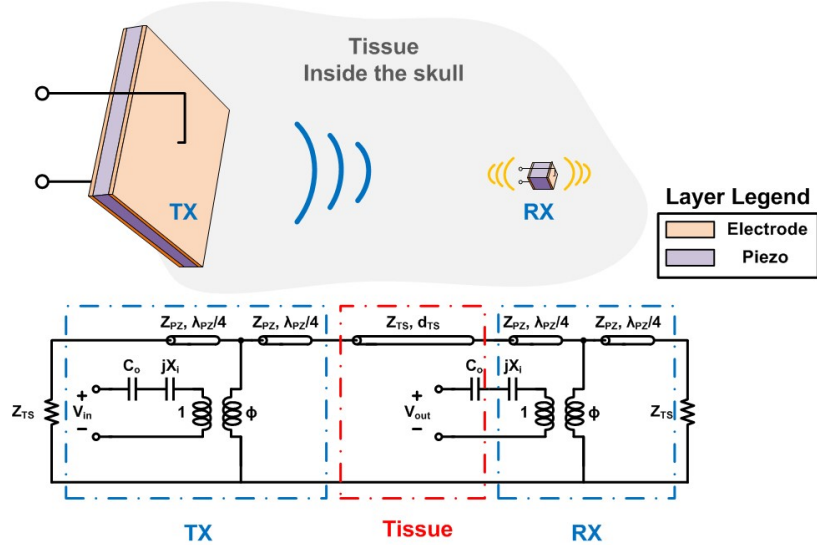


Figure 3.4. Complete single interrogator, single neural dust power and communication link models.

3.4.2 Complete link model

A good model of the ultrasonic channel is crucial in order to assess the tradeoffs in optimizing systems for power transfer through lossy brain tissue. The complete energy link model is shown in Figure 3.4 and can be divided into three parts: (1) the ultrasonic interrogator or *transmitter*, (2) tissue, and (3) the neural dust or *receiver*. A signal generator and amplifying stages produce power for the ultrasonic transmitter through an impedance matching circuit that provides conjugate matching at the input. The ultrasonic wave launched by the interrogator penetrates brain tissue, modeled as a lossy transmission line, and a fraction of that energy is harvested by the ultrasonic receiver, or neural dust. We evaluated embedding the receiver up to 2 mm into the tissue.

In order to compute the link power transfer efficiency, the model can be decomposed to a set of linear and time-invariant two-port parameters, representing a linear relationship between the input and output voltage. Here, we choose to represent the input-to-output relationship using ABCD parameters, which simplify analysis of cascades of two-port networks through matrix multiplication [43]. The cascaded ABCD parameters can then be

converted to Y-parameters using,

$$Y_{11} = \frac{D}{B}; Y_{12} = \frac{BC - AD}{B}; Y_{21} = \frac{-1}{B}; Y_{22} = \frac{A}{B} \quad (3.13)$$

and the power gain is defined as,

$$G_p = \frac{P_L}{P_{in}} = \left| \frac{Y_{21}}{Y_L + Y_{22}} \right|^2 \frac{Y_L}{Y_{in}} \quad (3.14)$$

where $Y_{in} = Y_{11} - \frac{Y_{12}Y_{21}}{Y_{22} + Y_L}$ and Y_L is the output load admittance.

3.4.3 Interrogator sizing

As the pressure field generated by a uniform continuous-wave excited piezoelectric transducer propagates through the tissue medium, the characteristics of the pressure field change with distance from the source. The varying field is typically divided into two segments, *near field* and *far field*. In the near field, the shape of the pressure field is cylindrical and the envelope of the field oscillates. At some point distal to the transducer, however, the beam begins to diverge and the pressure field becomes a spherically spreading wave, which decays inversely with distance. The transition between the near and far field is where the pressure field converges to a natural focus, and the distance at which this occurs is called the Rayleigh distance, defined as,

$$L = \frac{D^2 - \lambda^2}{4\lambda} \approx \frac{D^2}{4\lambda}, D^2 \gg \lambda^2 \quad (3.15)$$

where D is the aperture width of the transmitter and λ is the wavelength of ultrasound in the propagation medium [44]. In order to maximize the received power, it is preferable to place the receiver at one Rayleigh distance where the beam spreading is at a minimum. Therefore, with 2 mm of transmission distance and a resonant frequency of 12 MHz as shown in Figure 3.3 ($\lambda = 125 \mu\text{m}$), the maximum dimension of the external interrogator should be ~ 1 mm.

3.5 Simulation Results

Recall the problem specifications from the case study with EM power transfer in the previous chapter,

Implant (RX) size	100 μm^2
Interrogator (TX) size	1 mm^2
Transmission distance	2 mm
Transmission medium	Brain tissue

We are again interested in the following questions:

- What is the achievable power transfer efficiency?
- What is the absolute maximum power we can harvest at the implant?
- Does this approach scale to allow high density neural recordings?

The complete link model in Figure 3.4 with PZT is implemented in MATLAB with the limitations of the KLM model (as outlined in the previous section) corrected via COMSOL simulations. Given a 1 mm^2 interrogator, Figure 3.5 plots both the efficiency of the link and the received power (following track 3) at the sensor node as the size of the dust scales and the thickness of the interrogating transducer is adjusted to match the resonant frequency of the dust and the tissue. We note that the maximum efficiency of the KLM-adapted link model, where the interrogator is fully immersed in the tissue medium, is limited to 50 % because both the back and front side of the interrogator are loaded by the tissue layer. This results in an efficiency drop of 3 dB as the ultrasonic energy couples to both the front and back face of the transducer equally. Additionally, without any impedance matching, since the acoustic impedance of the tissue (1.5 MRayls) and that of PZT (30 MRayls) are drastically different, significant reflection occurs at their boundaries. Depending on the thickness of neural dust and the resonant frequency of the network, ultrasonic waves launched by the interrogator undergo varying phase changes through the lossy tissue. Thus, the efficiency of a system

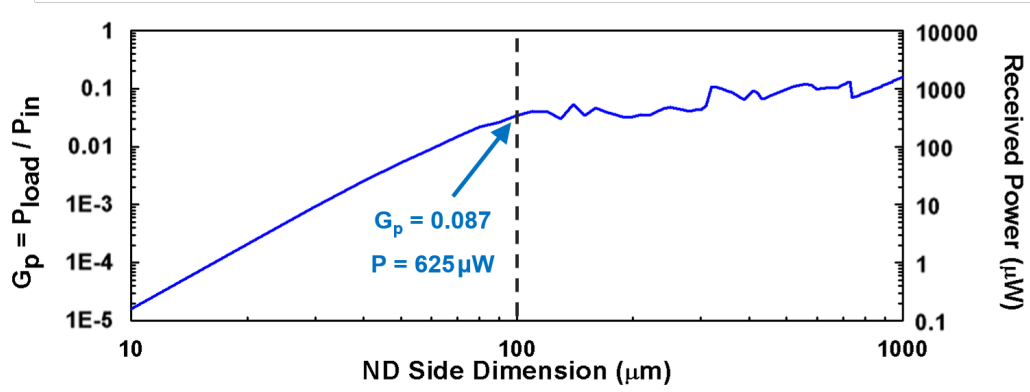


Figure 3.5. Link efficiency as a function of the neural dust side dimension.

with smaller dust nodes can be improved if the total propagation distance happens to be a multiple of a wavelength of the ultrasound. As a result, for dust nodes greater than 100 μm , we note that the efficiency does not monotonically increase with the dimension. On the other hand, for a dust node that is less than 100 μm in dimension, because the wavelength associated with the network's resonant frequency is much smaller than its tissue propagation distance, the link efficiency depends more heavily on the cross-sectional area of the dust. Therefore, we note that the efficiency will drop at least quadratically with the reduction of dust dimension.

More specifically, simulation of the complete link indicates that for a 100 μm node embedded 2 mm into the brain, ultrasonic power transmission can enable 8.7 % efficiency power transmission (-10.6 dB) with tissue attenuation of 0.5 dB/(cm·MHz). At the resonant frequency, we can receive up to $\sim 625 \mu\text{W}$ at the neural dust node (resulting in nano-meters of total displacement) with a 1 mm^2 interrogator, which is $\sim 10^8$ more than EM transmission at the same size scale (8 pW in Figure 2.1). Figure 3.6 illustrates the comparison between power transfer using EM and ultrasound, indicating that for implants smaller than $\sim 1 \text{mm}^2$, ultrasonic power transfer outperforms EM significantly.

Scaling of neural dust also indicates that approximately 5 μW can be recovered by a

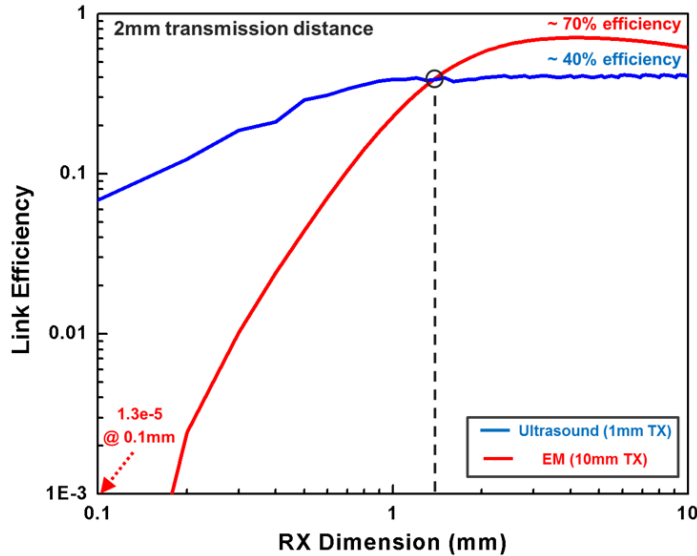


Figure 3.6. Comparison of link efficiency via EM and ultrasound indicates that for implants smaller than $\sim 1 \text{ mm}^2$, ultrasonic power transfer outperforms EM significantly.

dust node as small as $20 \mu\text{m}$ through ultrasonic transmission, which is still in the realm of feasibility to operate a state-of-the-art CMOS neural front-end.

3.6 Theoretical Scaling Limit

Free-floating extracellular recording at untethered, ultra-small dust nodes poses a major challenge in scaling. Unlike the needle-like microelectrode shanks that can measure time-domain electrical potential at each recording site in relation to a common electrode placed relatively far away, in neural dust both the recording and the common electrode must be placed within the same (very small) footprint. Although the two are interchangeable, the separation and therefore the maximum differential signal between the electrodes are inherently limited by the neural dust footprint, with the signal following the dipole-dipole voltage characteristic that decreases quadratically (unless very near a cell body, in which case it appears to scale exponentially; see [45] for a more thorough review) with increasing

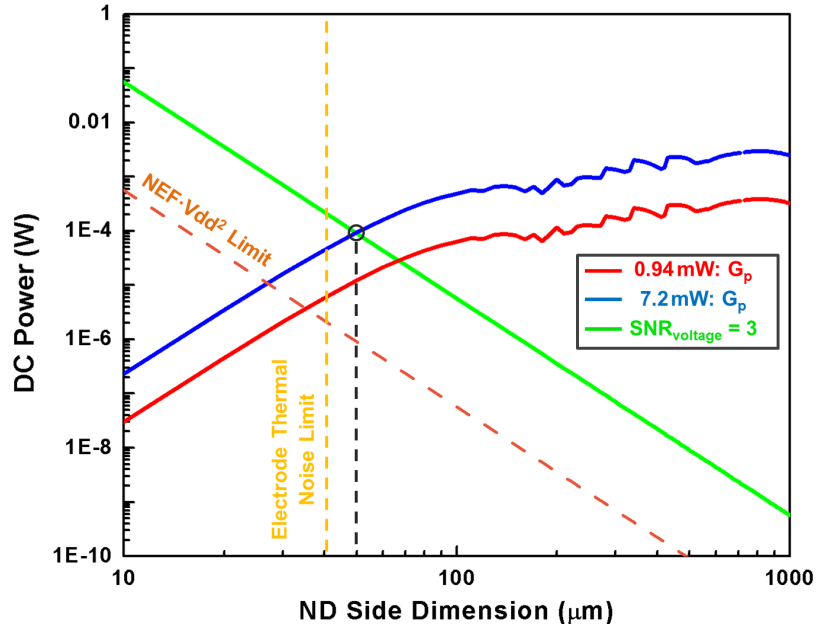


Figure 3.7. As we scale down neural dust dimension, more power is needed to keep the noise floor down to maintain SNR while less power is captured. The intersection of these two trends is the smallest node that will still operate. The analysis assumes the use of PZT, two different FDA-approved ultrasonic power transfer protocols.

separation distance. Since the power available to the implant has a fixed upper bound (see above), the reduction of extracellular potential amplitude as the neural dust dimensions are scaled down in the presence of biological, thermal, electronic and mechanical noise (which do not scale) causes the signal-to-noise (SNR) ratio to degrade significantly; this places heavy constraints on the CMOS front-ends for processing and extracting the signal from extremely noisy measurements. Therefore, if we consider sufficient SNR at the input of the neural front-ends as one of the design variables, the scaling of neural dust (as depicted in Figure 3.5) must be revisited.

Focusing specifically on the scaling of a cubic neural dust, at a separation distance of 100 μm between recording electrodes, we expect a 10 μV AP amplitude [data derived from [46]], with the amplitude further reducing quadratically as the separation is reduced. Since the power available to the neural dust is limited, the design goal of a front-end architecture is to minimize the input-referred noise within this power budget. The power efficiency

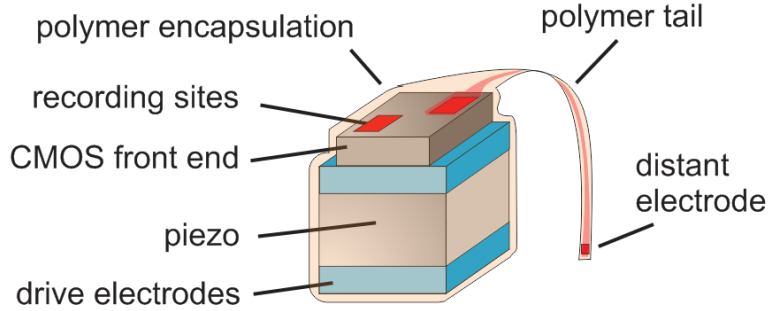


Figure 3.8. Neural dust with an ultra-compliant flexible polyimide “tail”, populated with recording sites, can be envisioned to bypass the limits of the achievable differential signal between two electrodes placed on a neural dust footprint and to extend the scaling limit.

factor ($\text{NEF}^2 \cdot V_{\text{dd}}$) quantifies the tradeoff between power and noise [47], and extrapolating from the measurement result of a previous CMOS neural front-end design ($\text{NEF}^2 \cdot V_{\text{dd}}$ of 9.42 [10]), we can estimate the relationship between the input-referred noise level and the DC power consumption of an optimally designed front-end architecture as we scale. The fundamental limit to the $\text{NEF}^2 \cdot V_{\text{dd}}$ occurs at a supply voltage of at least $\sim 4 \text{ kT}/q$ or 100 mV, in order to reliably operate the FET, and by definition, the NEF of 1 for a single BJT amplifier [48]. In principle, one could push the supply voltage down to $\sim 2 \text{ kT}/q$, but in practice 100 mV is already extremely aggressive.

Fixing the input SNR to 3, which should be sufficient for extracting neural signals, we can evaluate the scaling capability of neural dust as shown in Figure 3.7. We assumed the use of PZT in the model described in the section above. We also assumed that the interrogator’s output power is constrained by the two different FDA-approved ultrasonic power transfer protocols. We note that there exists an inherent tradeoff between the power available to the implant and the exponential increase in the power required to achieve an SNR of 3 with the reduction of spacing between the electrodes. The point of intersection in Figure 3.7 denotes the minimum size of neural dust that enables the operation of the complete link. For the stated assumptions, this occurs at $80 \mu\text{m}$, which is greater than the dimension at which the thermal noise from the electrode ($R = 20 \text{ k}\Omega$ and $\text{BW} = 10 \text{ kHz}$) limits further scaling. This effectively means dust nodes smaller than $50 \mu\text{m}$ cannot receive

enough power to distinguish neural activity from noise. Note that the cross-over assumes 100 % efficiency in the rectifier and zero overhead cost in the remaining circuitry, both of which will not be true in practice (i.e., the actual size limit will be larger than this).

The scaling of neural dust shown above is limited by the noise requirement of the front-end architectures, which is determined by the achievable differential signals between the electrodes. Decoupling the inherent tradeoff between the size of individual implants and the achievable SNR can improve the scaling of these implementations. Since the tradeoff derives directly not from the neural dust dimension, but from electrode separation, one approach may be to add very small footprint ($\sim 1 - 5 \mu\text{m}$ wide) “tails” which position a single (or multiple) electrodes relatively far ($> 50 - 100 \mu\text{m}$) from the base of the neural dust implant. This would result in the design shown in Figure 3.8, where instead of placing a single differential surface electrode on neural dust, the neural dust can consist of a short strand of flexible and ultra-compliant substrate populated with recording sites. Therefore, this approach can address one of the major pitfalls with only a minor adjustment to the original idea as this neural dust still operates under the same principle as before, but has higher achievable SNR.

Chapter 4

Experimental Verification

4.1 Introduction

In order to verify the results from the simulation framework, we assembled test boards using commercially available PZT sheets and performed experiments with a custom ultrasonic scanning system. This chapter outlines the experiment setup in detail and compares the measurement and simulation results.

4.2 Sample Preparation

4.2.1 Piezoelectric material

As described in the previous chapter, there are several different types of piezoelectric materials available for various applications. The majority of the piezoelectric ceramics or crystals contain lead to provide a boost in the piezoelectric performance. Non-lead alternatives, such as barium titanate (BaTiO_3) and lithium niobate (LiNbO_3) exist, but they are generally inferior to their PZT counterparts and therefore less widely used. A complete survey of piezoelectric materials and their properties can be found in the Appendix A.

A set of experiments presented in this thesis were carried out with PZT due to the relative ease of obtaining PZT crystals with varying geometry. Metalized PZT sheets of several thicknesses were obtained (PSI-5A4E, Piezo Systems, Woburn, MA and PZT 841, APC Internationals, Mackeyville, PA), with a minimum PZT thickness of 127 μm . The PZT was fully encapsulated in PDMS silicon for biocompatibility; the effect of the PDMS on performance will be discussed later.

4.2.2 PZT dicing

The most commonly used method to dice PZT ceramics is to use a wafer dicing saw with an appropriate ceramic blade to cut PZT sheets into individual PZT crystals. The minimum resolution of the cut is determined by the kerf of the blade and can be as small as 30 μm .

Another possible option is to use a laser cutter. Unlike the dicing saw, laser cutting realizes the cuts by focusing a high-power laser beam onto a material, which melts, vaporizes, removes, and scribes the piece. The precision of laser cutting can be down to 10 μm and is limited by the wavelength of the laser. However, for treating sensitive samples such as PZT ceramics, the temperature at the site of cuts can be damaging to the piezoelectric performance of the material. Excimer laser cutting of ceramics uses UV laser to cut with excimer from noble gases, but such laser cutter is extremely expensive and no suitable services are currently available. As a result, we rely on dicing saw to perform all the cuts.

4.2.3 Electrical connection

In order to drive or extract electrical energy from the PZT, we must make an electrical connection to both the top and bottom plates. The materials typically used as an electrode for PZT are silver or nickel. Silver is generally used for a wide variety of non-magnetic and AC applications and silver in the form of flakes suspended in a glass frit is usually screened onto the ceramic and fired. For high electric field DC applications, silver is likely to migrate

and bridge the two plates. As a result, nickel, which has good corrosion resistance and does not electro-migrate as readily can be electroplated or vacuum deposited as an alternative.

Both materials can be soldered onto with the appropriate solder and flux. For instance, silver is soluble in tin, but a silver loaded solder can be used to prevent scavenging of silver in the electrode. Phosphor content from the nickel plating can make soldering tricky, but the correct flux can remove surface oxidation. However, when soldering, in order to avoid exceeding the Curie point and depoling the PZT sample, the soldering temperature must be between 240 and 300 °C. Even at these temperatures, since the PZT is also pyroelectric, one must be careful not to exceed 2 - 4 seconds of soldering time.

Alternatively, an electrical connection can be made using either silver epoxy or low-temperature soldering using solder paste. Standard two-part silver epoxy can provide a sufficient electrical conductivity and can be cured even at room temperature overnight. However, the joints tend to be fragile and can easily break during testing. The bond can be reinforced by using a non-conductive epoxy as an encapsulation but this additional layer presents a mechanical load to the PZT and can significantly dampen its quality factor. Low-temperature solder paste on the other hand undergoes a phase change between the temperature of 150 and 180 °C and can provide great electrical connection and a bond strength that is comparable to that achieved with flash soldering . Therefore, we chose the low-temperature soldering approach.

4.2.4 Post-processing PZT

As described previously, wafer dicing is capable of cutting PZTs into small crystals of 10's of μm . However, samples that are smaller than 1 mm in dimension are extremely difficult to handle with tweezers and bond to. In addition, due to the variation in the length of wire used to interface with top and bottom plates of PZT crystals (and therefore parasitic inductance and capacitance introduced by the wire) and the amount of solder paste dispensed across a number of samples, the impedance spectroscopy measurements were inconsistent.

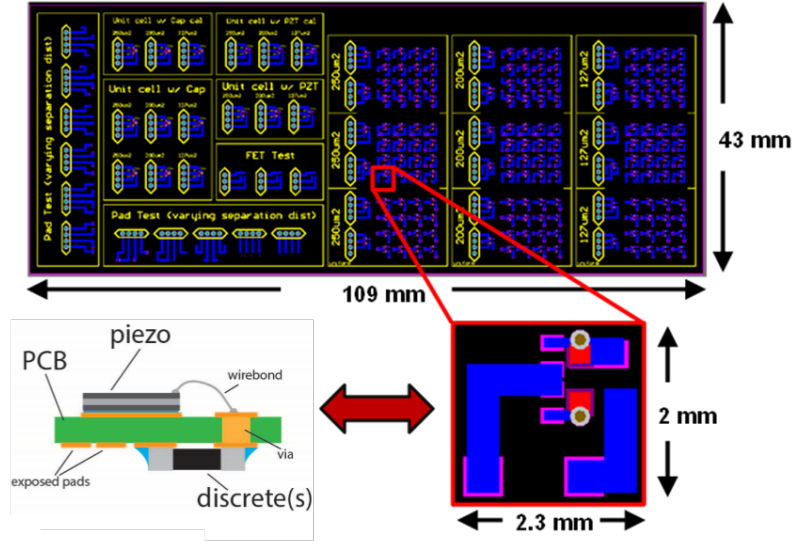


Figure 4.1. Assembly prototype schematic and PCB board for the experiments.

Therefore, we fabricated a 31 mil thick two-layer FR-4 PCB where we can have all of the electrical interconnects short and de-embed out the parasitics from the wires and the board. The fabricated board, which consists of numerous test structures and a module for individually characterizing $127\ \mu\text{m}$, $200\ \mu\text{m}$, and $250\ \mu\text{m}$ thick PZT crystals are shown with dimensions in Figure 4.1. Each unit cell in the test module contains two pads with specified dimensions on one side of the PCB to interface with the PZT crystals and pads for discrete components for backscattering communication on the opposite side [6]. The pitch between the unit cells is limited by the size of the discrete components and is roughly $2.3\ \text{mm} \times 2\ \text{mm}$.

In order to avoid directly handling tiny PZT crystals, Figure 4.2 outlines a scalable process flow to bond PZT onto the PCB,

1. Solder paste is dispensed using a pump at a constant pressure and for a controlled amount of time on one of the pads on the top side (details found in the Appendix A). The pads are either $250\ \mu\text{m}^2$, $200\ \mu\text{m}^2$, or $127\ \mu\text{m}^2$ based on the thickness of the PZT used.

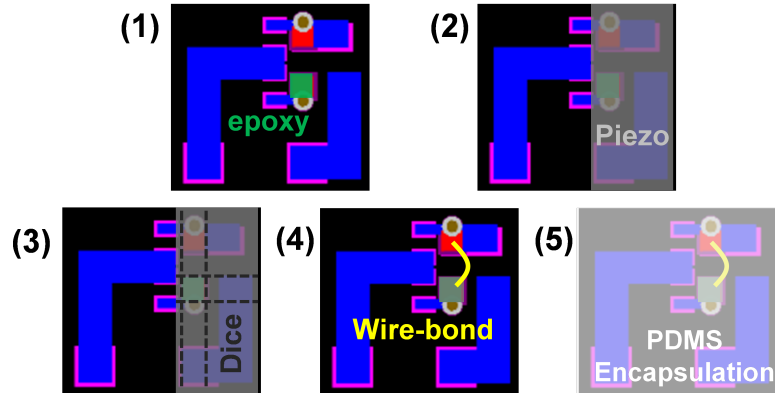


Figure 4.2. The processing steps ensure that the desired PZT dimension is assembled on the test board.

2. A PZT piece larger than the pad (that can be easily handled) is placed on top to cover the pads. The board and piezo assembly is baked in an oven to cure the solder paste. Therefore, PZT crystals are now bonded to pre-soldered bumped electrodes.
3. A wafer dicing saw makes a total of four cuts along the edges of the pad with the solder paste using alignment markers on the board, with non-bonded areas dropping off and leaving an array of small PZT crystals bonded to the PCB.
4. A single wirebond makes an electrical contact between the top plate of the PZT and an electrode on the PCB, completing the circuit.
5. Finally, the entire assembly is encapsulated in PDMS (Sylgard 184, Dow Corning, Midland, MI) to protect the wirebond and provide insulation.

Several process debugging steps and tips can be found in the Appendix A.

4.3 Top Level Outline of Design

Since piezoelectric material is an electro-mechanical structure, we need to characterize both its electrical and mechanical properties. In this section, we detail the test setup and techniques to perform such measurements.

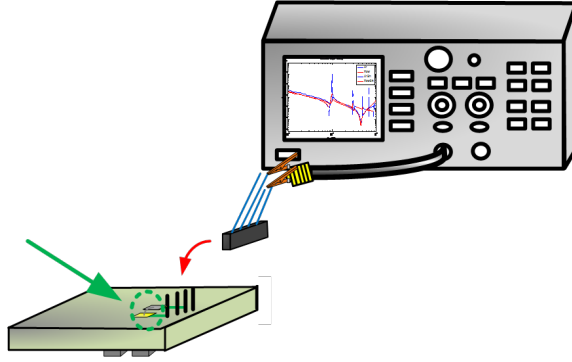


Figure 4.3. Measurement diagram for electrical impedance measurement with VNA.

4.3.1 Electrical characterization

Any electrical device can be modeled as a black box using a mathematical construct called two-port network parameters. The properties of the circuits are specified by a matrix of numbers and the response of the device to signals applied to its input can be calculated easily without solving for all the internal voltages and currents in the network. There are several different types of two-port network parameters, such as Z-parameters, Y-parameters, S-parameters, and ABCD-parameters, etc. and the conversion between different parameters can be easily derived [43]. The apparatus that enables us to extract these parameters is called a vector network analyzer (VNA). A VNA incorporates directional couplers to decompose the voltage in each port into incident and reflected waves (based on impedance mismatching), and calculate the ratio between these waves to compute scattering or S-parameters.

Before performing measurements using a VNA, one must calibrate the instrument since the internal directional couplers are non-ideal. Calibration also allows us to move the reference plane of the measurement to the tips of the cable, i.e., calibrate out parasitics from the cable. There are several calibration standards [43] but the most commonly used is open, short, and load calibration procedures. The measurement schematic is shown in Figure 4.3. Alligator clips, which are soldered onto the ends of the coaxial cable, are used to interface

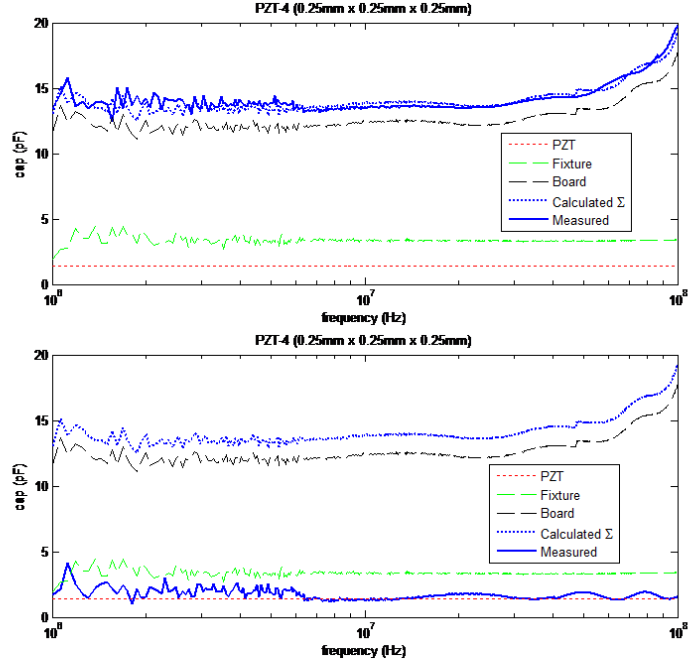


Figure 4.4. Before (top) and after (bottom) calibrating out the board.

with the top/bottom plates. The parasitics from the clips were not significant below 100 MHz.

As an example, we used a VNA (E5071C ENA, Agilent Technologies, Santa Clara, CA) to measure the electrical properties of a $(250 \mu\text{m})^3$ PZT crystal, shown in Figure 4.4. We note that the measured capacitance of the PZT crystal vastly differs from the capacitance we expect from a simple parallel-plate capacitance model due to significant parasitic capacitances from the PCB and the fixture (clip and connector). Since the VNA coefficients from the calibration step previously outlined only moved the measurement plane to the tips of the cable, we need to use open/short/load calibration structures fabricated on the same board to include the board and fixture parasitics. The result of full calibration is shown in Figure 4.4, where the measured PZT response matches the expected response.

Using this calibration technique, we can also plot the impedance of the PZT as a function of frequency, as shown in Figure 4.5. From this plot, however, it is extremely difficult to determine whether there is any electro-mechanical resonance. When we overlay the sim-

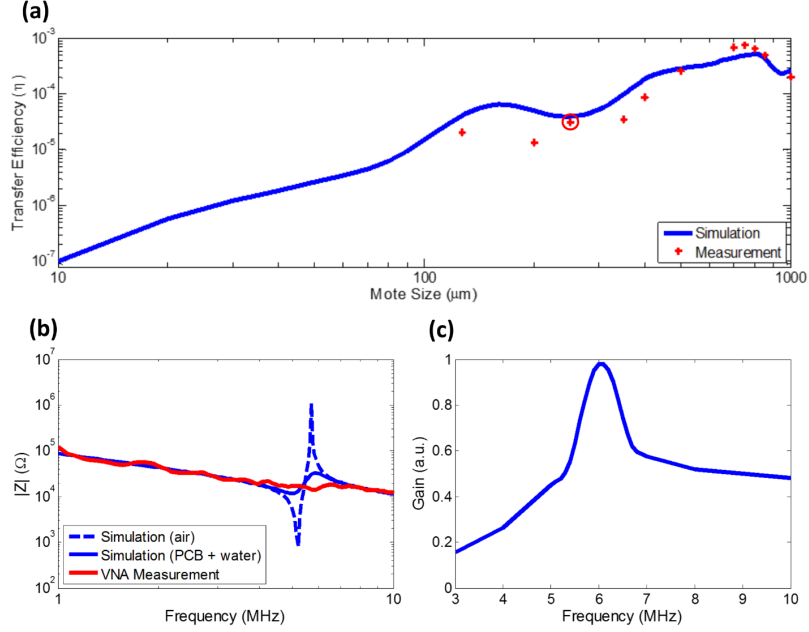


Figure 4.5. Measured impedance spectroscopy of a PZT crystal matches simulation.

ulation result with air backing (no mechanical clamping), we notice that the impedance spectroscopy matches well with the measurement at low and high frequencies, with the exception of noticeable peak at resonant frequency of roughly 6 MHz and its harmonics. When we clamp and load one side of PZT with PCB (FR-4), we see a significant dampening of the resonant peaks from air backing. Despite a lack of observable resonance in the measurement, we can make out a small blimp around 6 MHz and can calculate the mechanical quality factor Q_m using the following equations,

$$Q_m = \frac{f_a^2}{2_r Z_r C_p (f_a^2 - f_r^2)} \quad (4.1)$$

where f_a and f_r represent anti-resonant (where impedance is maximized) and resonant frequency (where impedance is minimized), Z_r represents an impedance at resonance, and C_p is the low-frequency capacitance. The calculated quality factor from the measurement is roughly 4.2 compared to 5.1 in simulation. According to the datasheet, the unloaded Q of the PZT is ~ 500 , indicating that FR-4 backing and wire-bonds are causing significant degradation of the quality factor. Despite the drastic reduction in the mechanical Q of the

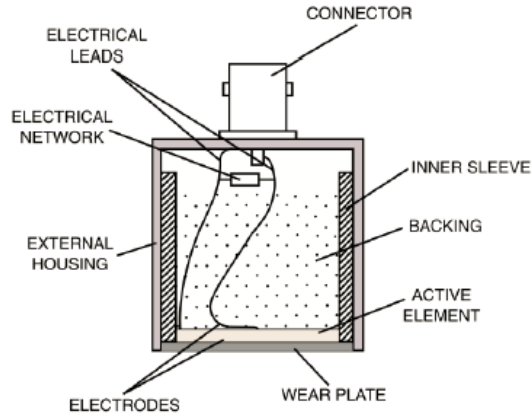


Figure 4.6. Cross section of an ultrasonic transducer

PZT crystals, experiments showed that the backscattered signal level only decreased by roughly ~ 19

4.3.2 Ultrasonic characterization

In the electrical characterization setup, the VNA has a built-in signal generator to provide the input necessary for characterization. In order to perform acoustic characterization of PZT, we must first be able to generate and launch acoustic waves onto the sample to use as an input. This can be achieved with commercially available broadband ultrasonic transducers.

Figure 4.6 shows the composition of a representative transducer, which consists of a piezoelectric active element, backing, and wear plate. The backing is usually made from a material with high attenuation and high density to control the vibration of the transducer by absorbing the energy radiating from the back face of the active element while the wear plate is used to protect the transducer element from the testing environment and to serve as a matching layer.

Ultrasonic power transfer tests were performed using the home-built setup shown in

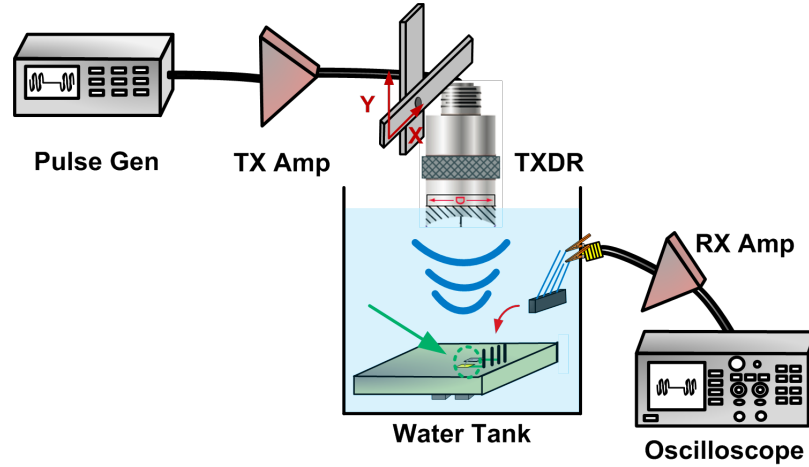


Figure 4.7. Acoustic characterization setup with a calibrated ultrasonic transducer for power delivery verification

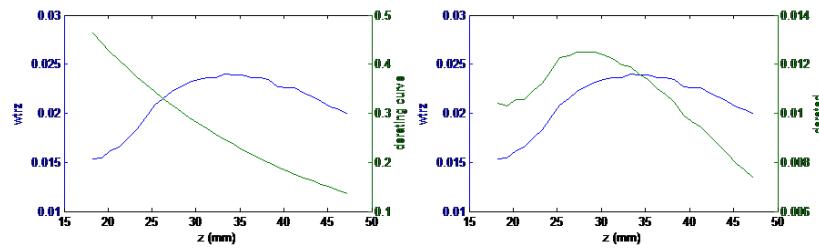


Figure 4.8. The output power of a 5 MHz transducer as the hydrophone is moved away from the transducer’s surface. The de-rated peak is shifted to the left in relation to the water peak.

Figure 4.7. A 5 MHz or 10 MHz single element transducer (6.3 and 6.3 mm active areas, respectively; ~ 30 mm focal distance; Olympus, Waltham, MA) was mounted on a computer-controlled 2-axis translating stage (VelMex, Bloomfield, NY). The transducer’s output was calibrated using a hybrid capsule hydrophone (HGL-0400, Onda, Sunnyvale, CA). Assembly prototypes were placed in a water container such that transducers could be immersed in the water at a distance of approximately 3 cm directly above the prototypes. A programmable pulse generator (33522B, Agilent Technologies, Santa Clara, CA) and radio frequency amplifier (A150, ENI, Rochester, NY) were used to drive transducers at specified frequencies with sinusoidal pulse trains of 10-cycles and a pulse-repetition fre-

quency (PRF) of 1 kHz. The received signals were amplified with with a radio frequency amplifier (BT00500-AlphaS-CW, Tomco, Stepney, Australia), connected to an oscilloscope (TDS3014B, Tektronix, Beaverton, OR) to collect ultrasound signals and record them using MATLAB. Pictures of the measurement setup can be found in the **Appendix**.

4.4 Experimental Results

Figure 4.8 shows a representative measurement of the output power of the 5 MHz transducer as a function of the distance between the surface of the transducer to the hydrophone (z -axis). The peak pressure in water was obtained at ~ 33 mm away from the transducer’s surface while the de-rated peak (with 0.3 dB/cm/MHz) was at ~ 29 mm. Figure 4.9 shows the de-rated XZ scan of the transducer output, which shows both near-field and far-field beam patterns and a Rayleigh distance or a focal point at ~ 29 mm, matching Figure 4.8. Figure 4.10 shows a XY cross-sectional scan of the beam at the focal point of ~ 29 mm, where the 6 dB beamwidth measured roughly 2.2 mm.

The total integrated acoustic output power of the transducer at various frequencies over the 6 dB bandwidth of the beam was nominally kept at a spatial-peak temporal-average I_{SPTA} of $29.2 \mu\text{W}/\text{cm}^2$, resulting in a total output power of $\sim 1 \mu\text{W}$ at the focal point, with a peak rarefaction pressure of 25 kPa and a mechanical index (MI) of 0.005. Both the de-rated I_{SPTA} and MI were far below the FDA regulation limit of $720 \text{ mW}/\text{cm}^2$ and 1.9, respectively (FDA, 2008).

Figure 4.11 shows the measured power delivery efficiency of the fully assembled prototype with cable loss calibrated out for various neural dust node sizes as compared to analytical predictions made for this same setup. Measured results matched the simulated model behavior very closely across all node sizes, with the exception of a few smaller node dimensions, likely due to the sensitivity to transducer position and the ultrasound beamwidth. The measured efficiency of the link for the smallest PZT crystal ($127 \mu\text{m}$)³ was 2.064×10^{-5} , which resulted in 20.64 pW received at the dust node nominally. A maximum of $0.51 \mu\text{W}$ can be recovered at the dust node if the transmit output power density was kept

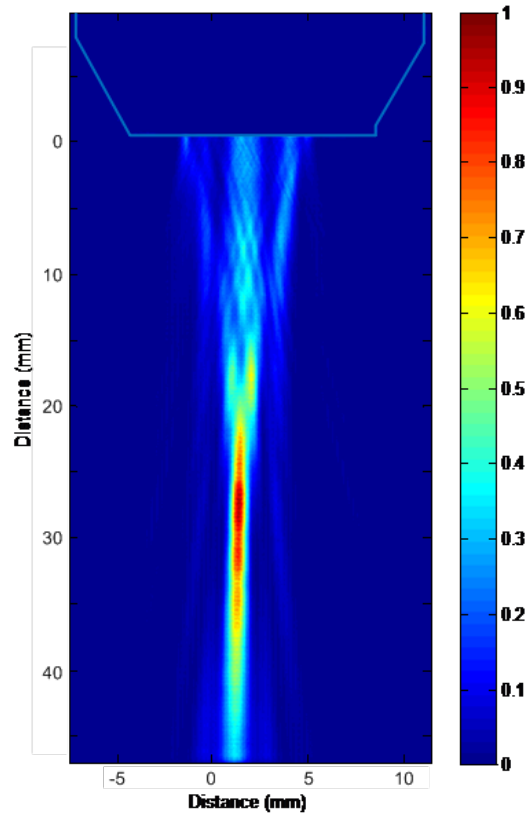


Figure 4.9. The XZ cross-section of the transducer output illustrates a Rayleigh distance and a clear transition from the near-field to far-field propagation.

at 720 mW/cm^2 . Such low power level harvested by the PZT is mainly due to the extreme inefficiency of broadband transducers that were used for the experiments; dedicated, custom-made transducers at each node dimension with optimal electrical input impedance could result in more than 2 orders of magnitude improvement in the harvested power level as predicted by the simulation model.

The frequency response of electrical voltage harvested on a $(250 \text{ }\mu\text{m})^3$ PZT crystal is shown in Figure 4.12 We measured the resonant frequency to be at 6.1 MHz, which matches the shift in the resonant frequency predicted for a cube due to Poisson's ratio and the associated mode coupling between resonant modes along each of the three axes of the

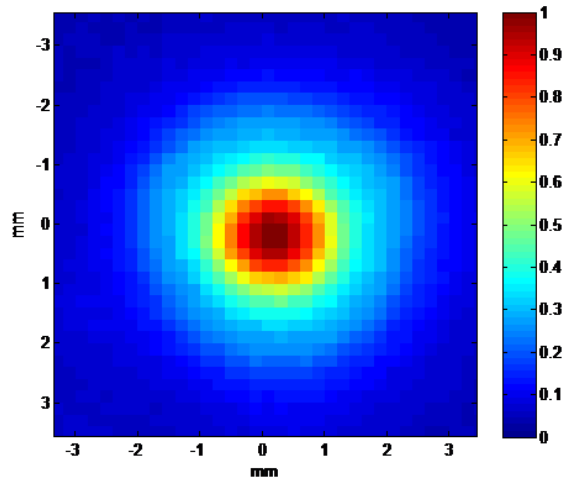


Figure 4.10. The XY beam cross-section shows 6 dB bandwidth of the beam at 2.2 mm.

cube, as discussed previously. Furthermore, the calculated Q of 4.8 matched the electrically measured Q of the PZT.

4.5 Summary

The experimental results indicate that the analytical model for power coupling to very small PZT nodes using ultrasound is accurate down to at least $\sim 100 \mu\text{m}$ scales and likely lower. It remains to be seen just how small a node can be fabricated before loss of function.

Note that measurements of even smaller nodes ($< 127 \mu\text{m}$) were limited not by the prototype assembly process, but by commercial availability of PZT substrates. Moving forward, we are harnessing the considerable volume of research and techniques that has gone into micro- and nanoelectromechanical RF resonators [49], [50] and thin-film piezoelectric transducers [51] to facilitate extremely small (10's of μm) dust nodes and to truly assess the scaling theory.

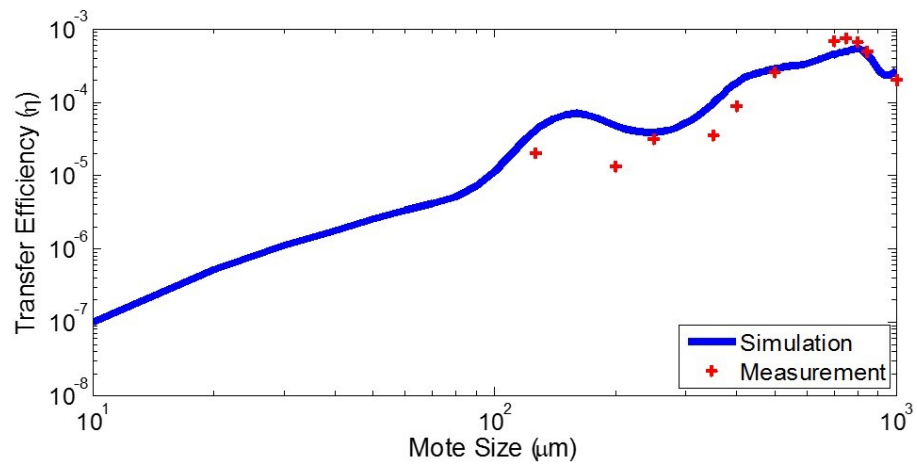


Figure 4.11. Measured power transfer efficiency at various neural dust sizes matches simulated behavior closely.

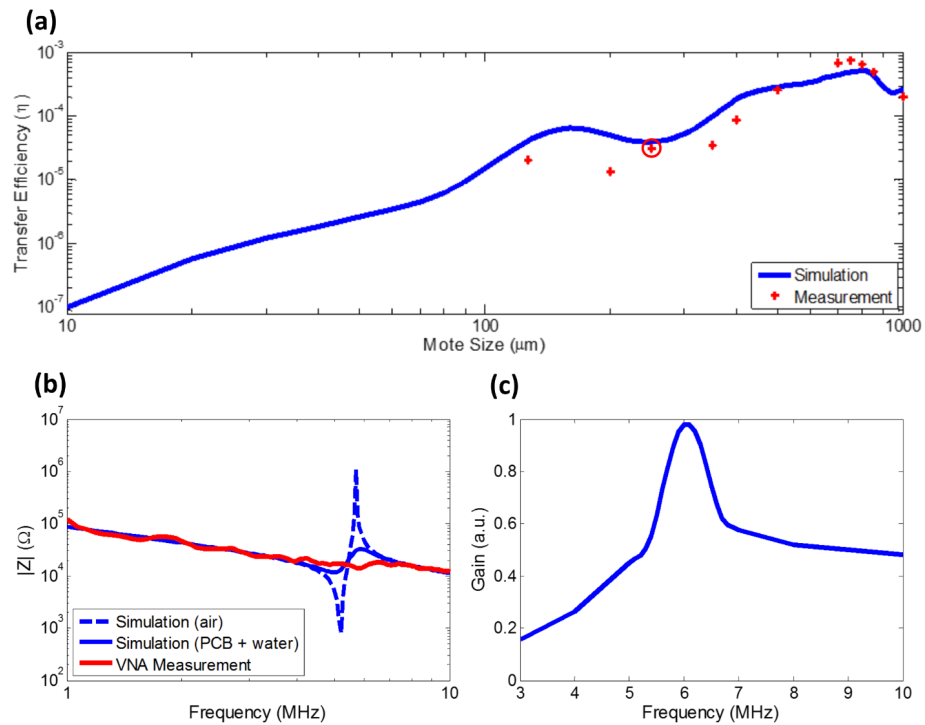


Figure 4.12. Frequency response of harvested power on the PZT reinforces the reliability of the simulation framework.

Chapter 5

Conclusion

5.1 Thesis Summary

Currently, a major hurdle in brain-machine interfaces (BMI) is the lack of an implantable neural interface system that remains viable for a lifetime due to the development of biological response near the electrode. Recently, sub-mm implantable EM-based wireless neural interfaces have been demonstrated in an effort to extend system longevity, but the implant size scaling (and therefore density) is ultimately limited by the power available to the implant.

This work presents a new method of wireless power telemetry using ultrasound, which can address fundamental issues associated with using EM to interrogate miniaturized implants. It details the system design trade-offs and ultimate size, power, bandwidth scaling limits, as well as a process flow to fabricate sub-mm size, untethered neural recording devices powered by ultrasound.

The proposed system improves the power transfer efficiency by up to 8 orders of magnitude compared to the traditional EM-based neural recording devices at the same size scale and can be engineered to operate down to 10's μm scales, comparable to one or two cell diameters. The extreme scalability of an ultrasound-based neural recording system makes

it an attractive candidate to realize a seamless, high density, chronic interface to the human brain for clinically relevant applications such as BMI.

5.2 Future Directions

The analysis presented points to four major challenges.

The first is the design and demonstration of front-ends suitable for operating within the extreme constraints of decreasing available power and decreasing SNR with scale. This could be addressed with a combination of CMOS process and design innovation as well as thinned, multi-substrate integration strategies.

The second challenge is the integration of extremely small piezoelectric transducers and CMOS electronics in a properly encapsulated package. The above discussion assumed the entire neural dust implant was encapsulated in an inert polymer or insulator film (a variety of such coatings are used routinely in neural recording devices; these include parylene, polyimide, silicon nitride and silicon dioxide, among others) while exposing two recording electrodes to the brain.

An implementation strategy to enable ultrasonic backscatter communication with a single node is also required. Beyond that, the third challenge arises in the design and implementation of an array of suitably sensitive sub-cranial interrogators which can operate at low power (to avoid heating between skull and brain) and can enable multi-dust and multi-interrogator communications strategies which make use of modern communication techniques such as beam steering and multi-input, multi-output (MIMO) system theory. An alternative approach to multi-node communication would be to fabricate dusts with a variety of resonant frequencies and use frequency discrimination (i.e., each dust transmits on its own frequency channel).

Lastly, there is the additional problem of how to deliver neural dust nodes into the cortex. The most direct approach would be to implant them at the tips of fine-wire arrays similar to those already used for neural recording. Neural dust nodes would be fabricated or

post-fab assembled on the tips of array shanks and held there by surface tension or resorbable layers; a recent result demonstrates a similar approach to implant untethered LEDs into neural tissue [52]. Once inserted and free, the array shanks would be withdrawn, allowing the tissue to heal. Kinetic delivery might also be an option, but there is no existing data to evaluate what effect such a method would have on brain tissue or the devices themselves.

References

- [1] Chapin JK, Markowitz R, Moxon KA, Nicolelis MAL (1999) Direct real-time control of a robot arm using signals derived from neuronal population recordings in motor cortex. *Nat Neurosci* 2:664-70.
- [2] Serruya MD, Hatsopoulos NG, Paninski L, Fellows MR, Donoghue JP (2002) Instant neural control of a movement signal. *Nature* 416:141-2.
- [3] Carmena JM, Lebedev MA, Crist R, O'Doherty JE, Santucci DM, et al. (2003) Learning to control a brain-machine interface for reaching and grasping by primates. *PLoS Biol* 1:e42. doi:10.1371/journal.pbio.0000042.
- [4] Ganguly K, Carmena JM (2009) Emergence of a stable cortical map for neuroprosthetic control. *PLoS Biol* 7: e1000153. doi:10.1371/journal.pbio.1000153.
- [5] Koralek KC, Jin X, Long JD, Costa RM, Carmena JM (2012) Corticostriatal plasticity is necessary for learning intentional neuroprosthetic skills. *Nature* 483:331-5.
- [6] Seo D, Carmena JM, Rabaey JM, Alon E, Maharbiz MM (2013) Neural dust: An ultrasonic, low power solution for chronic brain-machine interfaces. *arXiv:1307.2196*.
- [7] Venkatraman S, Carmena JM (2011). Active sensing of target location encoded by cortical microstimulation. *IEEE Trans Neural Syst Rehabil Eng* 19:31724.
- [8] O'Doherty J, Lebedev M, Ifft P, Zhuang K, Shokur S, Bleuler H, Nicolelis M (2011). Active tactile exploration using a brain-machine-brain interface. *Nature* 479:22831.
- [9] Marblestone AH, Zamft BM, Maguire YG, Shapiro MG, Cybulski T, Glaser JI, Stranges PB, Kalhor R, Dalrymple DA, Seo D, Alon E, Maharbiz MM, Carmena JM, Rabaey JM, Boyden ES, Church GM, Kording KP (2013) Physical Principles for Scalable Neural Recording. *Front in comp neuro* 7.
- [10] Biederman W, Yeager DJ, Narevsky N, Koralek AC, Carmena JM, Alon E, Rabaey JM (2013) A Fully-Integrated, Miniaturized (0.125 mm²) 10.5 μ W Wireless Neural Sensor. *IEEE J Solid-State Circuits* 48(4):960-70.
- [11] Miranda H, Gilja V, Chestek CA, Shenoy KV, Meng TH (2010) HermesD : A High-Rate Long-Range Wireless Transmission System for Simultaneous Multichannel Neural Recording Applications. *IEEE Trans BioCAS* 4(3):181-91.
- [12] Szuts TA, et al. (2011) A wireless multi-channel neural amplifier for freely moving animals. *Nat Neurosci* 14(2):263-9.
- [13] Fan D, et al. (2011) A wireless multi-channel recording system for freely behaving mice and rats. *PLoS One* 6(7): 1-9.
- [14] Stevenson I, Kording K (2011) How advances in neural recording affect data analysis. *Nat Neurosci* 14(2):139-42.

- [15] Nicolelis MAL, Dimitrov D, Carmena JM, Crist R, Leheew G, Kralik JD, Wise SP (2003) Chronic, multisite, multielectrode recordings in macaque monkeys. *Proc Natl Acad Sci* 100:11041-6
- [16] Harrison RR, Watkins PT, Kier RJ, Lovejoy RO, Black DJ, Greger B, Solzbacher F (2007) A Low-Power Integrated Circuit for a Wireless 100-Electrode Neural Recording System. *IEEE J Solid-State Circuits* 42(1):123-33.
- [17] Turner JN, Shain W, Szarowski DH, Andersen M, Martins S, Isaacson, M, Craighead H (1999) Cerebral astrocyte response to micromachined silicon implants. *Experimental Neurology* 156:33-49.
- [18] Polikov VS, Tresco PA, Reichert WM (2005) Response of brain tissue to chronically implanted neural electrodes. *J Neurosci Met* 148:1-18.
- [19] Chestek CA, et al. (2011) Long-term stability of neural prosthetic control signals from silicon cortical arrays in rhesus macaque motor cortex. *J Neural Engineering* 8:1-11
- [20] Suner S, Fellows MR, Vargas-Irwin C, Nakata GK, Donoghue JP (2005) Reliability of signals from a chronically implanted, silicon-based electrode array in non-human primate primary motor cortex. *IEEE Trans on NeuralSRE* 13(4):524-41.
- [21] Alivisatos AP, et al. (2013) Nanotools for neuroscience and brain activity mapping. *ACS Nano* 7(3):1850-66.
- [22] Rabaey JM, et al. (2011) Powering and communicating with mm-size implants. *IEEE DATE Conf* 1-6.
- [23] Sodagar AM, Amiri P (2009) Capacitive coupling for power and data telemetry to implantable biomedical microsystems. *IEEE EMBS Conf* 411-4.
- [24] Lee SB, Lee H, Kiani M, Jow U, Ghovanloo M (2010) An inductively powered scalable 32-channel wireless neural recording system-on-a-chip for neuroscience applications. *IEEE Trans BioCAS* 4(6):360-71.
- [25] Yakovlev A, Kim S, Poon A (2012) Implantable biomedical devices: Wireless powering and communication. *IEEE Comm Mag* 50(4):152-9.
- [26] Clark GM (2003) Cochlear implants: fundamentals and applications. *New York: Springer-Verlag*.
- [27] IEEE (2006) C95.1-2005 IEEE Standard for Safety Levels with Respect to Human Exposure to Radio Frequency Electromagnetic Fields, 3 kHz to 300 GHz.
- [28] Mohan SS, Mar Hershenson M, Boyd SP, Lee TH (1999) Simple accurate expressions for planar spiral inductances. *IEEE J Solid-State Circ* 34(10):1419-24.
- [29] Jow UM, Ghovanloo M (2007) Design and Optimization of Printed Spiral Coils for Efficient Transcutaneous Inductive Power Transmission. *IEEE BioCAS* 1(3):193-202.
- [30] Ishida K, et al. (2013) Insole Pedometer With Piezoelectric Energy Harvester and 2 V Organic Circuits. *IEEE J Solid-State Circuits* 48(1):255-64.

- [31] Wong SH, Kupnik M, Butts-Pauly K, Khuri-Yakub BT (2007) Advantages of Capacitive Micromachined Ultrasonics Transducers (CMUTs) for High Intensity Focused Ultrasound (HIFU). *IEEE Ultrasonics Symp*:1313-6.
- [32] Ozeri S, Shmilovitz D (2010) Ultrasonic transcutaneous energy transfer for powering implanted devices. *Ultrasonics* 50(6):556-66.
- [33] Richards CD, Anderson MJ, Bahr DF, Richards RF (2004) Efficiency of energy conversion for devices containing a piezoelectric component. *J Micromech Microeng* 14:717-21.
- [34] Rosen CA, Fish KA, Rothenberg HC (1958) Electromechanical Transducer. US patent no. 2830274.
- [35] Hoskins PR, Martin K, Thrush A, editors (2010) Diagnostic Ultrasound: Physics and Equipment. *New York: Cambridge University Press*.
- [36] Leighton TG (2007) What is ultrasound? *Progress Biophysics & Molecular Biology* 93:3-83.
- [37] FDA (2008) Information for Manufacturers Seeking Marketing Clearance of Diagnostic Ultrasound Systems and Transducers.
- [38] Zenner HP, et al. (2000) Human studies of a piezoelectric transducer and a microphone for a totally implantable electronic hearing device. *Am J Otol* 21(2):196-204.
- [39] Maleki T, Cao N, Song S, Kao C, Ko SA, Ziaie B (2011) An ultrasonically powered implantable micro-oxygen generator (IMOG). *IEEE Trans BioE* 58(11):3104-11.
- [40] Krimholtz R, Leedom DA, Matthaei GA (1970) New equivalent circuits for elementary piezoelectric transducers. *Electronics Lett* 6(13):398-9.
- [41] Roa-Prada S, Scarton HA, Saulnier GJ, Shoudy DA, Ashdown JD, Das PK, Gavens AJ (2013) An Ultrasonic Through-Wall Communication (UTWC) System Model. *J Vib Acoust* 135(1):1-12.
- [42] Holland R (1968). Resonant properties of piezoelectric ceramic rectangular parallelepipeds. *J Acoust Soc Am* 43(5):988-97.
- [43] Pozar DM (2011) Microwave engineering. *John Wiley and Sons*.
- [44] Kino GS (1987) Acoustic waves: devices, imaging, and analog signal processing. *Prentice Hall*.
- [45] Gold C, Henze DA, Koch C (2007) Using extracellular action potential recordings to constrain compartmental models. *J Comput Neurosci* 23:39-58.
- [46] Du J, Blanche TJ, Harrison RR, Lester HA, Masmanidis SC (2011) Multiplexed, high density electrophysiology with nanofabricated neural probes. *PLoS One* 6(10):1-11.
- [47] Muller R, Gambini S, Rabaey JM (2012) A 0.013 mm² 5 μ W DC-coupled neural signal acquisition IC with 0.5 V supply. *IEEE J Solid-State Circuits* 47(1):232-43.
- [48] Steyaert MSJ, Sansen WM, Zhongyuan C (1987) A micropower low-noise monolithic instrumentation amplifier for medical purposes. *IEEE J Solid-State Circuits* 22(6):1163-8.

- [49] Sadek AS, Karabalin RB, Du J, Roukes ML, Koch C, Masmanidis SC (2010) Wiring nanoscale biosensors with piezoelectric nanomechanical resonators. *Nano Lett* 10:1769-73.
- [50] Lin Y, Li S, Ren Z, Nguyen CTC (2005) Low phase noise array-composite micromechanical wine-glass disk oscillator. *IEEE Elec Dev Meeting* 1-4.
- [51] Trolier-McKinstry S, Muralt P (2004) Thin film piezoelectrics for MEMS. *J Electroceram* 12:7-17.
- [52] Kim T, et al. (2013) Injectable, Cellular-Scale Optoelectronics with Applications for Wireless Optogenetics. *Science* 340:211-6.

Acknowledgements

I would like to thank Dr. Patrick Goodwill, Dr. Paul Lum, Daniel Hensley (UC Berkeley), and Prof. Mikhail G. Shapiro (Caltech) for ultrasound equipment and test setup advice, Filip Maksimovic (UC Berkeley) for help with hydrophone measurements, and Dr. Peter Ledochowitsch (Allen Institute) and Dr. Alexander Bertrand (KU Leuven) for valuable discussions. Lastly, I would like to thank the support provided by a Graduate Fellowship from the NSF.

Appendix A

Appendix

A.1 Table of Piezoelectric Materials

Refer to the Table A.1.

A.2 Process Debugging

A.2.1 Electroplating

Electroplating is the deposition of positively charged metal particles, or ions, moving through a solution by electricity, attracting them onto an object that has been given a negative charge. Since we cannot wirebond directly to nickel (electrode material for 127 μm PZTs), we electroplated gold onto it.

We performed tank plating, where a container full of a alkaline cyanide free gold plating solution that contains dissolved gold (as an electrolyte) and stainless steel anode were used. Temperature of the solution was maintained at 140 – 200 °F. The required current density was 0.005 A/sq in, so the current supply was adjusted accordingly to the size of the part. After exposing the part for 30 – 60 seconds, we rinsed the part thoroughly in distilled water and dried it completely.

Refer to the Table A.2 below for troubleshooting.

A.2.2 PZT dicing

Given the desired dimensions of the PZT crystals and the pitch between the elements, the PZT sheets are anchored to the PCB only at a few bond sites, with the rest of the space underneath filled with air. Additionally, given the stiffness of the PZTs, when the wafer dicing saw is lowered to execute cuts, mechanical stress and reverberation from the blade can cause the PZTs to crack. In order to prevent this and provide support to the voids, we use *crystal bond* as an under-fill, which melts/flows at 121 °C and hardens as it cools. Since crystal bond is quite viscous (similar to runny glue), it is quite difficult to flow crystal bond under the PZTs once the PZTs are bonded. Therefore, we simply cut some scraps

		PZT-4	PZT-5H	BaTiO ₃	PVDF	LiNbO ₃	PMN-PT
		"Hard" ceramic	"Soft" ceramic	Traditional ceramic	Piezoelectric polymer	Traditional single crystal	New, high performance single crystal
Stiffness	c_{33}^D (GNm ⁻²)	155	159	110	8.52	251	135
Density	ρ (kgm ⁻³)	7500	7500	5550	1760	4640	8000
Velocity	v (ms ⁻¹)	4560	4600	5640	2200	7360	4040
Acoustic Z	$Z = \rho v$ (MRayl)	34.1	34.5	31.3	3.92	34.1	32.3
Strain const	d_{33} (pmV ⁻¹)	289	593	120	25	5.88	1430
Voltage const	g_{33} (mVmN ⁻¹)	26	20	16.8	230	22	30
Thickness mode coupling	k_t	0.508	0.512	0.42	0.19	0.162	0.566
Permittivity (zero strain)	ϵ_{33}^S	638	1470	1000	10-12	29	818
Mechanical Q	Q	High	Medium	Medium	Low	Very High	Low

Figure A.1. Table of Piezoelectric Materials

Problem	Cause	Remedy
Parts not plating	<ul style="list-style-type: none"> Poor connections 	<ul style="list-style-type: none"> Check all wiring
Parts turn dark grey or black	<ul style="list-style-type: none"> Power supply is reversed Current is too high 	<ul style="list-style-type: none"> Positive must go to anode Reduce the current
Parts turn hazy, cloudy, or dark	<ul style="list-style-type: none"> Current is too high Temperature is too high Solution is used up 	<ul style="list-style-type: none"> Reduce the current Reduce the solution temperature Replace the solution
Parts are dark and not plated	<ul style="list-style-type: none"> Current is too low Not plated long enough Solution is old 	<ul style="list-style-type: none"> Increase the current Increase the plating time Replace the solution
Parts are too rich in gold color	<ul style="list-style-type: none"> Current is too high 	<ul style="list-style-type: none"> Reduce the current or plate for a shorter time

Figure A.2. Troubleshooting for electroplating

using an x-acto and place them around the solder paste before placing the PZT sheets on top as shown in Figure A.3. Crystal bond can be removed easily by re-heating or placing the PCB in an acetone bath (which does not affect the PCB).

A.3 Measurement Setup

Figure A.4 shows two separate measurement stations for characterizing transducer beam pattern and measuring the power transfer efficiency to neural dust nodes. The detailed measurement schematics can be found in Chapter 4.3. The following sections will show pictures of each test setup.

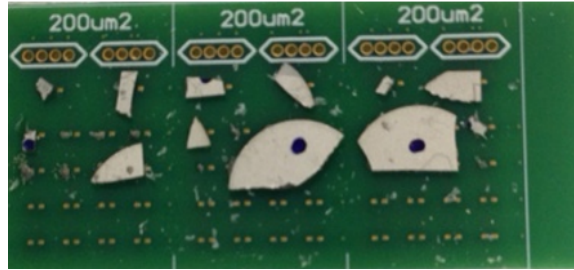


Figure A.3. Pieces of crystal bond surrounding the solderpaste (underneath the PZT sheets) pre-bake.

A.3.1 Hydrophone measurement

Refer to the Figure A.5, A.6, A.7 for pictures of the setup.

A.3.2 Power transfer measurement

Refer to the Figure A.8, A.9, A.10 for pictures of the setup.

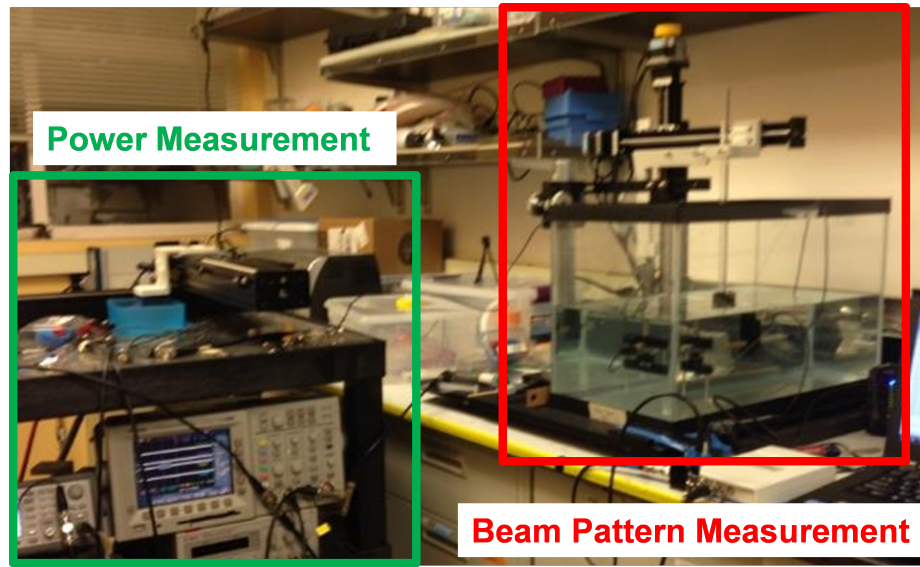


Figure A.4. Experimental stations for measuring neural dust power transfer efficiency (left) and transducer characterization (right).



Figure A.5. Ultrasonic transducer and the hydrophone are immersed in a water tank and mounted on 3-axis linear, computer-controlled and manual stages, respectively, for XYZ beam scanning.



Figure A.6. 1 - 20 MHz broadband hybrid capsule hydrophone has an active area of $400 \mu\text{m}$ at the tip, with 160 nV/Pa conversion. The hydrophone is attached to a switchable gain amplifier to increase its dynamic range.

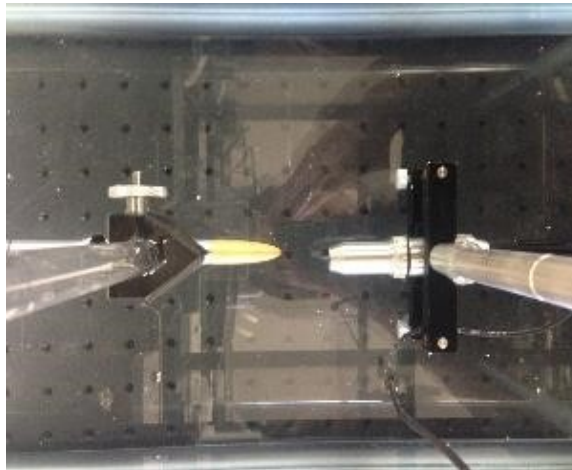


Figure A.7. The top view of the alignment of transducer to the hydrophone in the water tank. Due to the small aperture size of the hydrophone, the measurements are extremely vibration sensitive. Cautionary measures, such as using a vibration isolation workbench or pads, must be considered.

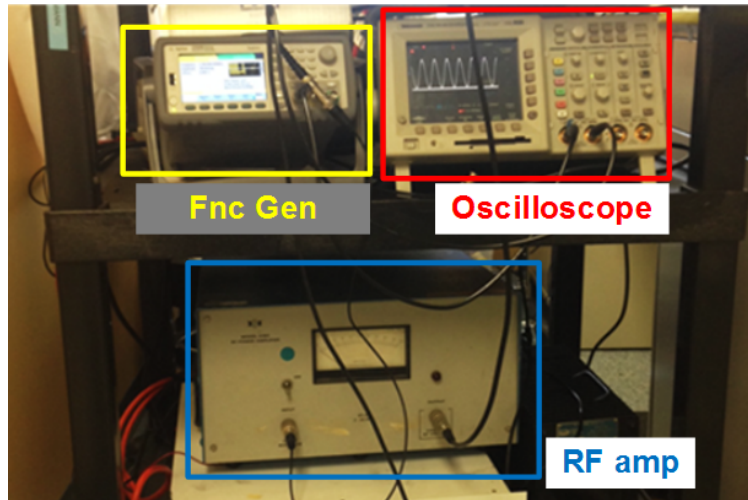


Figure A.8. A programmable function generator (in yellow) and radio frequency (RF) amplifier (in blue) were used to drive the ultrasonic transducer. The harvest voltage was displayed on the oscilloscope (in red).

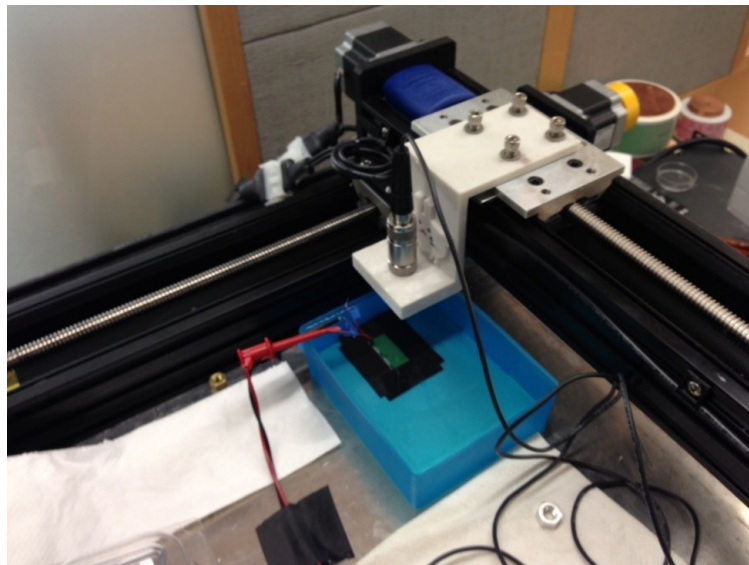


Figure A.9. The transducer is mounted on a computer-controlled 2-axis translating stage such that the transducer could be immersed in the water at a distance of approximately 30 mm directly above the sample.

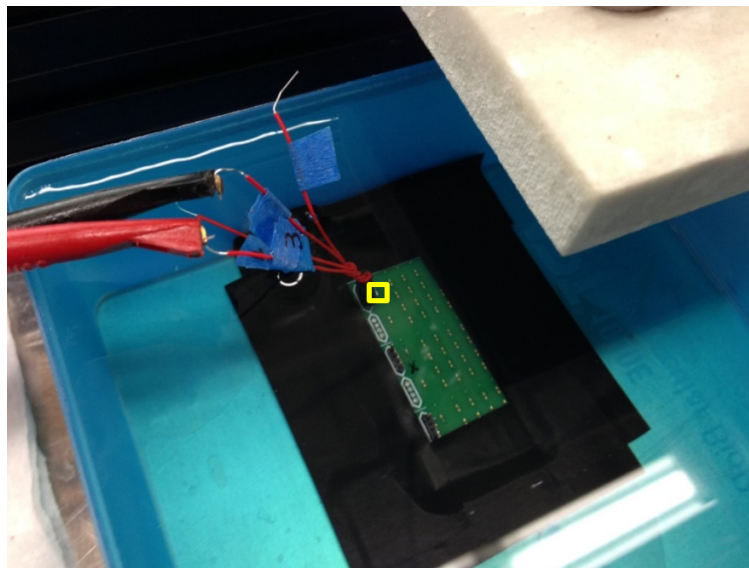


Figure A.10. Assembly prototype (PZT crystal in yellow) is placed in a water container and the power harvested by the piezo is displayed on an oscilloscope (not shown).